Stine Sandbakk

# Graphene Oxide Coatings for Anti-Fouling Applications

August 2020

NTNU
Norwegian University of
Science and Technology
Faculty of Natural Sciences
Department of Materials Science and Engineering

Master's thesis

2020

Stine Sandbakk

Master's thesis

NTNU
Norwegian University of
Science and Technology

NTNU
Norwegian University of
Science and Technology

NTNU
Norwegian University of
Science and Technology

# Graphene Oxide Coatings for Anti-Fouling Applications

Stine Sandbakk

Chemical Engineering and Biotechnology
Submission date: August 2020
Supervisor: Hilde Lea Lein
Co-supervisor: Sidsel Meli Hanetho

Norwegian University of Science and Technology
Department of Materials Science and Engineering

# Acknowledgements

As the world faced a pandemic earlier this year, it became clear that the conclusion to my Master's degree would not go as planned or be as expected. The society locked down, we suddenly got a favourite digital meeting platform and a preferred disinfection producer. It has been a different and challenging semester, but luckily I have been surrounded by a great bunch of supporting people.

First of all I want to thank my supervisor Hilde Lea Lein for all the guidance, motivational support and for being thoroughly positive. I know you are one busy woman, but you always have time for your master students and our weekly meetings. Thanks to my co-supervisor Sidsel Meli Hanetho at SINTEF Industry, for helpful advises on my laboratory work, valuable discussions regarding my results and all the fancy coffee machine coffee.

I want to thank my research group, Functional Material and Material Chemistry Group, for the feedback and comments on my work through presentations in our weekly meetings, and for allowing me to take part in fellow Master's students and Ph.D. candidates research. It has been utterly inspiring.

A huge thanks is given to all scientific and technical staff being a part of this thesis. In particular I want to thank Head Engineer Anita Storsve for keeping an eye on my experiments during campus lock down, to always find a solution to my problems in the laboratory, and for having the most infectious laughter I know. And to Senior Engeneer Agnes Digranes, for spending hours figuring out the AFM with me. We made it in the end and I am so grateful for your help. I also want to thank Ph.D candidates Viviann Hole and Ole Håvik Bjørkedal for their help on the XRD analysis.

Thanks to SINTEF Ocean for lending us the biofilm reactor, and to Senior Research Scientist Matilde Skogen Chauton (SINTEF Ocean) for her advice on experimental set-up and for teaching me about algae. To CealTech AS for providing us the graphene oxide material, and to fellow classmates for discussions, confessions and lots of laughter over digital coffee breaks.

I am not sure if my family deserves a thanks or an apology. Home office, unpredictable working days and occasionally drops in motivation may have effected both mood and charm in a not so positive manner. Your support was, and is, very much appreciated.

And Mari, this piece of paper would probably not existed if it was not you who introduced me to the world of chemistry. Your enthusiasm is infectious.

# Preface

This thesis is submitted to the Norwegian University of Science and Technology in the course TMT4900 Materials Chemistry and Energy Technology, Master's Thesis, as a part of the Master of Science degree in Materials Science. The course concludes the Master's degree program Chemical Engineering and Biotechnology at the Department of Material Science and Engineering (IMA). The work was preformed at the Functional Material and Materials Chemistry Group (FACET), with Associate Professor Hilde Lea Lein as supervisor. The work has been supported by SINTEF Industry, where Research Scientist Sidsel Meli Hanetho has served as co-supervisor. The examined Graphene Oxide material, was provided by the company CealTech AS.

All work has been performed in the laboratories at the Department of Materials Science and Engineering (IMA). The author has conducted most of the laboratory and characterization work presented in this thesis, except the X-Ray Diffraction analysis. The XRD experiments were conducted in cooperation with Ph.D. candidates Viviann Hole (IMA) and Ole Håvik Bjørkedal (IKP). The literature review is partly adapted and modified from earlier work by the author, in the Materials Technology, Specialization Project, on the same topic. Adapted parts are commented in the corresponding sections.

Trondheim, 14 August 2020

Stine Sandbakk

# Abstract

Coatings for anti-fouling application serve the ability to prevent algae growth on constructions in marine industries; in shipping, offshore industries, fish farming and water treatment. Today, copper oxide is widely used for anti-fouling purposes. It is highly toxic for water living organisms and accumulation in the food chains are of concern. Hence, it is highly relevant to find a less harmful substitute. Graphene materials exhibit growth inhibiting properties through different proposed mechanisms, where oxidative stress (excess of free radicals) in organisms is the most believed explanation. Graphene oxide makes it possible to utilize an anti-fouling agent without any harmful elements that also provides good mechanical properties, in order to reduce both environmental hazards and maintenance cost.

The object of this thesis was to synthesize anti-fouling coatings and compare the effect of graphene oxide (GO) and copper(II)oxide (CuO). The sol-gel process was utilized to synthesize a silica sol (from Tetraethyl Orthosilicate monomers), where anti-fouling agents were added. CuO did not disperse in the sol, leaving the final coating heterogeneous and agglomerated, and the examined results were not comparable to the GO coatings.

Coated steel substrates were characterized with respect to surface structure (SEM), topography (AFM), wetting (contact angle measurements), and adhesion strength (micro scratch tester). GO increases coating adhesion and improve strength. Compared to the reference silica coating and CuO coatings, the contact angle measurements showed a more hydrophobic character of the GO coatings. This was explained by chemical composition and surface roughness. Roughness were found to increase for increasing concentrations of GO.

Several biofilm experiments were performed on spray coated polyethylen (PE) substrates, and the experiments were run for one to four weeks. The abiotic factors (temperature, current and light access) were kept constant for all experiments, only varying the access of nutrients. From the one week experiments it was not possible to draw a conclusion upon the effects of GO as anti-fouling agent. In the four week experiment, the GO additive, was found to reduce the growth after a period of two weeks. The GO coating containing 0.015 GO/TEOS weight ratio (C-150) exhibits the best growth inhibiting properties, reducing bacteria growth with approximately 83%. Oxidative stress is believed to be the dominating antibacterial mechanism in the GO material.

The experimental procedure proved successful to prepare a GO coating suitable for determination of the anti-fouling properties in GO.

# Sammendrag

Belegg (coatinger) med grohindrende egenskaper har evnen til å hemme algevekst på konstruksjoner i marine næringer, i skipsfart, offshoreindustri, fiskeoppdrett og vannrensing. I dag brukes kobberoksid i flere relaterte belegg for å unngå vekst av alger. Kobberoksid er svært giftig, med fare for langtidsvirkninger, for organismer i vann. Akkumulasjon av kobber i marine miljø og næringskjeder er uønsket, og det er derfor svært relevant å finne en mindre skadelig erstatning. Grafénmaterialer viser veksthemmende egenskaper gjennom flere foreslåtte mekanismer, der oksidativt stress (overskudd av frie radikaler) i organismer er den best begrunnede forklaringen. Grafénoksid gjør det mulig å bruke et veksthindrende middel uten skadelige elementer som også har gode mekaniske egenskaper, for å redusere både miljøfarer og vedlikeholdskostnader.

I denne oppgaven var målet å syntetisere veksthemmende coatinger og sammenligne de grohindrende egenskapene til grafénoksid (GO) og kobber(II)oksid (CuO). Sol-gel metoden ble brukt til å syntetisere en silikacoating basert på tetraetylortosilikat-monomerer, hvor grohindrende middel ble tilsatt. CuO suspensjonene dannet ikke stabile dispersjoner og den ferdig coatede overflaten ga en heterogen og agglomerert overflate. Resultatene for disse coatingene er ikke sammenlignbare med resultatene for GO coatingene.

Belagte stålsubstrater ble karakterisert med hensyn på overflatestruktur (SEM), topografi (AFM), fukting (kontaktvinkermålinger) og adhesjonsstyrke (skrapetester). GO forbedrer adhesjonsegenskapene og styrken til coatingen. Sammenlignet med silika- og kobberoksidcoatinger viser kontaktvinkelmålinger at GO har dårligere fuktingsegenskaper. Dette forklares fra ruheten til overflaten, som øker med økende konsentrasjon av GO.

Flere biofilmeksperimenter ble gjennomført på belagte polyetylen (PE) substrater, og eksperimentene ble kjørt i én til fire uker. De abiotiske parameterene (temperatur, vannstrøm og lystilgang) ble holdt konstante, mens tilgangen til næring varierte. Fra eksperimentene på én uke, var det ikke mulig å trekke en konklusjon angående effekten av GO som grohindrende materiale. I forsøket kjørt i fire uker, viste GO å redusere bakterieveksten etter en periode på to uker. GO coatingen, med vektforholdet 0.015 GO/TEOS (C-150), viste de beste grohindrende egenskapene og reduserte bakterieveksten med omtrent 83%. Oksidativt stress er antatt å være den dominerende antibakterielle mekanismen i GO materialet.

Den eksperimentelle prosedyren viste seg å være vellykket med tanke på å fremstille et GO-belegg som er egnet for bestemmelse av grohindrende egenskaper i GO.

# List of Abbreviations

| | | |
|---|---|---|
| AF | - | Anti-Fouling |
| AFM | - | Atomic Force Microscopy |
| CA | - | Contact Angle |
| CuO | - | Copper(II)Oxide |
| DIW | - | De-Ionized Water |
| EDS | - | Energy-Dispersive X-Ray Spectroscopy |
| EtOH | - | Ethanol |
| FR | - | Fouling Release |
| GMs | - | Graphene Materials |
| GO | - | Graphene Oxide |
| MIC | - | Microbiological Induced Corrosion |
| OM | - | Optical Microscope |
| PE | - | Polyethylen |
| rGO | - | Reduced Graphene Oxide |
| RT | - | Room Temperature |
| ROS | - | Reactive Oxygen Species |
| SEM | - | Scanning Electron Microscopy |
| TEM | - | Transmission Electron Microscopy |
| TEOS | - | Tetraethyl Orthosilicate |
| XRD | - | X-Ray Diffraction |

# Contents

# 1 Introduction

## 1.1 Background

Biofouling cause material damage and represent a challenge in cost, maintenance and efficiency on constructions and equipment exposed to the marine environment [1]. There are several cases of damage caused by fouling; in shipping, offshore industry, aquaculture and in water treatment. In fish farms, biological foulants accumulate on fish nets and prevent oxygen from entering the cage and compromise fish welfare and reduce biomass production. Biofouling on vessel hulls increases the hydrodynamic drag and as a consequence, the fuel consumption increases. Fouling on oil and gas infrastructure or power plants might damage sensitive equipment as cooling systems and membranes and can cause failure. Prevention of accumulation of biofoulants is important for all marine industries and activities operating in seawater or coastal areas where biofouling can occur, illustrated in Figure 1.1.

**Figure 1.1:** Captions of biofouling from maritime industries. The pictures visualize fouling on fish nets (top left), membrane (bottom left) and vessel hull (right). Images are modified from [2, 3, 4]

Inorganic additions to paint might serve as anti-fouling (AF) agent and is a coating strategy to avoid algal growth on construction surface. The additives can be tailored to form strong bonds to the surrounding matrix, forming a composite coating, designed for the desired application.

Copper oxide is widely used for anti-fouling purposes and is the biocide of choice for present day anti-fouling paint [5, 6]. It is highly toxic for water living organisms and accumulation belonging food chains are of concern. CuO paint is the major source of copper being introduced to the marine environment. Hence, it is relevant to find a less harmful substitute.

Graphene materials are reported to provide anti-fouling properties and excellent mechanical strength, and are promising materials for anti-fouling use [7]. Graphene oxide is found to have the lowest cytotoxicity among the graphene materials [8, 9]. This makes graphene oxide a promising alternative as additive in anti-fouling coatings.

## 1.2 Aim of Work

The aim of this project is to achieve a greater understanding of the anti-fouling mechanisms in graphene oxide (GO), how it behaves and can be utilized in anti-fouling paint application. The aim is to prepare coatings based on a silica sol with graphene oxide and copper(II)oxide as additives, and then compare the anti-fouling effect of the two, based on methods established in the specialization project [10].

The first objective is to synthesize a silica coating by a sol gel process and characterize the sol properties by Fourier transform infrared (FTIR) spectroscopy, viscosity and visual appearance. The additive materials will be characterized by X-ray diffraction (XRD), scanning electron microscopy (SEM), FTIR- and Raman spectroscopy.

Optimization of additive concentrations and coating thickness to obtain a homogeneous, crack-free surface will be established in the second objective. The coating will be applied to substrates by spray coating as deposition technique. To obtain an understanding of how the addition of graphene oxide affect the material properties, a thorough study of surface structure, physical and chemical analysis will be preformed. SEM, atomic force microscopy (AFM), cross sectional EDS analysis, micro scratch tests and contact angle measurements are methods to be used for coating characterization.

The last and most important objective to this work is to test coating resistance to biofilm growth, by leaving the coated substrates in a biofilm reactor over time, varying the levels of enriched seawater medium (f/2). SEM will be utilized as characterization method for biofilm assessments.

# 2 Literature Review

## 2.1 Introduction to Biofouling

Biofouling is the process of accumulation of unwanted biological material at an interface [11]. Structured microbial communities that develop on solid surfaces within an aqueous phase, is called biofilms. Biofilm development is dependent on substrate, environmental conditions and biofilm composition. Bacterial adhesion, or attachment, is the first and most important step of the biofilm development, followed by the steps of biofilm formation, growth and detachment [12]. Bacteria adheres to the surface by long range forces (van der Waal forces), before short range forces (H-bonds) attaches it and create stronger bonds at the surface. Once adhered, the microorganisms form a biofilm, which is a matrix-encased community, specialised for surface persistence. This attachment is irreversible [13].

### 2.1.1 Marine biofilms

In ecology the concept of succession has a central place. It includes species replacements and change in composition or structure of ecological communities [14]. It is characterized in two phases, primary and secondary, depending on the extent of colonization. Introduction of submerged structures like oil and gas platforms, ship hulls or fish nets to the sea, represent unfouled surfaces witch are rapidly colonized through primary succession. An open space is a key resource for most sessile marine organisms, providing a site for attachment and further potential access to other key resources, like light and nutrients. Hence, any artificial substrata introduced to the marine environment are quickly colonised with different species of micro- and macro-algae [15].

There are four general phases of marine fouling colonisation: Adsorption of dissolved organic molecules, colonisation of procaryotes, colonisation of unicellar eucaryotes, followed by recruitment of larvae and algal spores [15, 16]. The phases can occur sequentially, overlap or occur in parallel [17, 18]. Metals, plastics, organic materials and living tissue are all surfaces suffering from adhesion of bacteria and microalgae. It is initiated by deposition of a slimy, polymer layer called extracellular polymeric substances (EPS),

containing saccharides, proteins and nucleic acids [19]. Not all proteins and polysaccarides present in the water absorb equally to the same substrate, which may inhibit or facilitate microbial attachment character [17]. Already adhered organisms may stimulate or suppress co-adhesion of other planktonic microorganisms, that further stimulates formation of multispecies heterogenous biofilms [20]. A schematic overview illustrating the biofilm attachment process is provided in Figure 2.1.

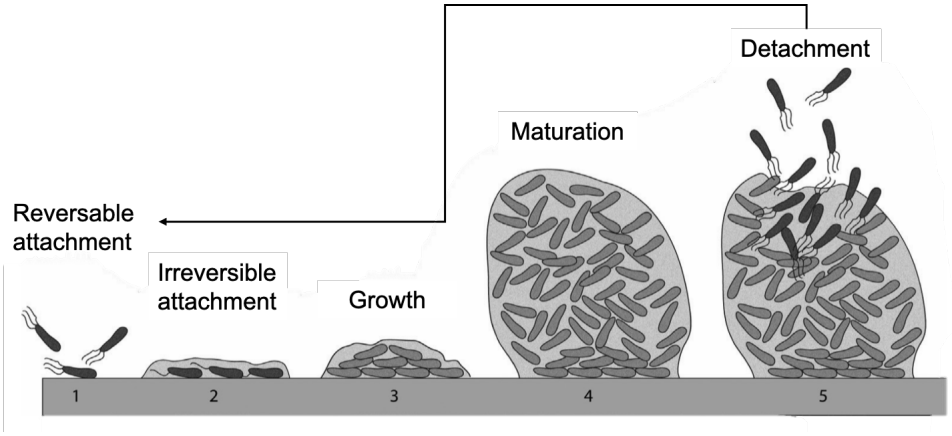


**Figure 2.1:** A schematic overview illustrating the life cycle of a biofilm on a clean surface, from surface attachment to growth and detachment [21].

The adhesion of microorganisms depends on several factors, as the substrate surface free energy, substrate properties and water current [22]. Most microorganisms attach more strongly to hydrophobic materials [16]. Surface roughness and hydrodynamic regime are other physical factors that affect the initial steps in the biofilm formation [23]. A number of investigations show that developed biofilm structures are affected by different physical factors (flow rate, hydrodynamic forces, substrate properties, viscosity), chemical factors (polymer deposition, nutrient availability) and biological factors (competition, predation).

### 2.1.2 Microbiological induced corrosion

A biofilm (from $\sim$ 100 $\mu$m thick) cause several industrial problems related to decrease in energy efficiency (increased drag, and corrosion. Microbiologically induced corrosion (MIC) can be caused by several mechanisms, including chatodic and anodic depolarisation, hydrogen production, metal reduction and production of metabolites such as organic acids and exopolymers [24]. A known corrosion process caused by biofilms is ennoblement of stainless steel. In this process the biofilm induce an increase in the open circuit potential towards positive (noble) values by metal reduction at the cathode. Oxygen is removed and acid is produces.

## 2.2 Graphene Materials

### 2.2.1 Material properties

Graphene is a $sp^2$ hybridized, two-dimensional monolayer carbon material, where pi-bonds are formed between electron clouds in the 2pz orbital, giving graphene its high conductivity and high surface energy [25]. This provides good electrical and thermal properties. The bond strength in the carbon sheets is high, giving GMs its excellent mechanical strength. Due to these superior properties, graphene have a significant impact on the field of materials science and nanotechnology, with graphene now being considered to replace various materials used in existing applications [26]

Graphene materials are of interest in composite materials due to its diverse properties. Composite technology is widely used in engineering, for example by introducing a harder material as an additive to a softer material. Experimental work show that graphene materials has the ability to achieve an increase in Young's modulus [27], tensile strength [28] and increase fracture toughness [29] in composites and composite coatings.

### 2.2.2 Graphene oxide

Graphene oxide (GO) is a monolayer hexagonal carbon lattice (graphene), with attached oxygen groups. The oxygen groups present in the structure are carboxyl edge group, and hydroxyl, carbonyl and epoxide groups in the basal plane. The extent of oxygen groups determines solubility and toxic effects in GO (and GMs generally) [30].

GO is often prepared by Hummer's method. It is a solution-based oxidation of graphene and is an attractive production route for its easy operation. In Hummer's method, potassium permanganate (the oxidation agent) is added to a solution of graphite, sodium nitrate, and sulfuric acid. The reaction time is relatively short compared to other methods for graphene oxidation, and it is a safe experiment not involving any toxic byproducts [31].

#### GO dispersion stability

The thermal movements in a solution is the driving force for equalization in concentration. At equilibrium, the molecules or particles are statistical distributed in the accessible volume, and are in a state of maximal entropy. In a system with concentration gradients, the Brownian movements will be considered as diffusion on a macroscopic level [32]. Graphene oxide form a metastable dispersion system in water, which means they are thermodynamically unstable, but might be stable for a limited period of time. In every colloidal system, Brownian movements will lead to collision between dispersed particles. If two particles approach and the attractive forces (van der Waals) get larger than the

repulsive forces(electrostatic and steric) their kinetic identity cease, cohesion occur and they form aggregates.

### 2.2.3 Raman spectroscopy for characterization of graphene-based materials

Raman spectroscopy is a fast, nondestructive, high resolution tool in characterization of graphene related carbon system. The spectroscopy method provides several important applications for quantification of solid state properties [33]. The Raman spectrum can determine defect density, doping levels, number of layers, quantify edge structures and the electronic structure. This by analyzing the peak position (P), line shapes (Lorenzian or Fano), full width at half maximum (FWHM, Γ), peak intensities (I) and peak area (A) [34].

A Raman spectrum for graphene oxide shows four main peaks, called the D, G, D' and 2D peaks. The distinct graphene materials characteristics are determined by these peaks. The D peaks refer to a disordered, diamond structure with $sp^3$-bonds, and the G peak is the graphite structure peak with $sp^2$-bonds. Structural and crystalline defects occurs during the synthesis process, and they deconstruct the selection rules that determine the Raman active modes in $sp^2$-bonded graphene systems [33]. Disordered graphene activates more phonon modes, but their features are broadened by the defects. Spectral deconvolution is a method to extract phonon modes or determine sub bands from Raman spectra. To obtain high precision in the investigation, the constrained non-linear method (CNM) is a suggested deconvolution method [35].

## 2.3 Synthesis of Silica Coatings

The following chapter is adapted and modified from previous work [10].

### 2.3.1 Introduction to sol-gel synthesis

The solution gelation (sol-gel) process is a simple and cost-efficient method for production of dense coatings and thin films [36]. In the method, a precursor is mixed with water in a solvent. When water is added a hydrolysation reaction takes place. An acid or base is added as a catalyst, depending on desired reaction mechanism and wanted polymer structure. The next step in the sol-gel process is the gelation step, where a condensation reactions forms oxide or alcohol bridges in a network formation. Hydrolysis and condensation reactions for tetraethyl orthosilicate (TEOS) are found in Figure 2.1. Reaction b) is the abundant condensation reaction in this work.

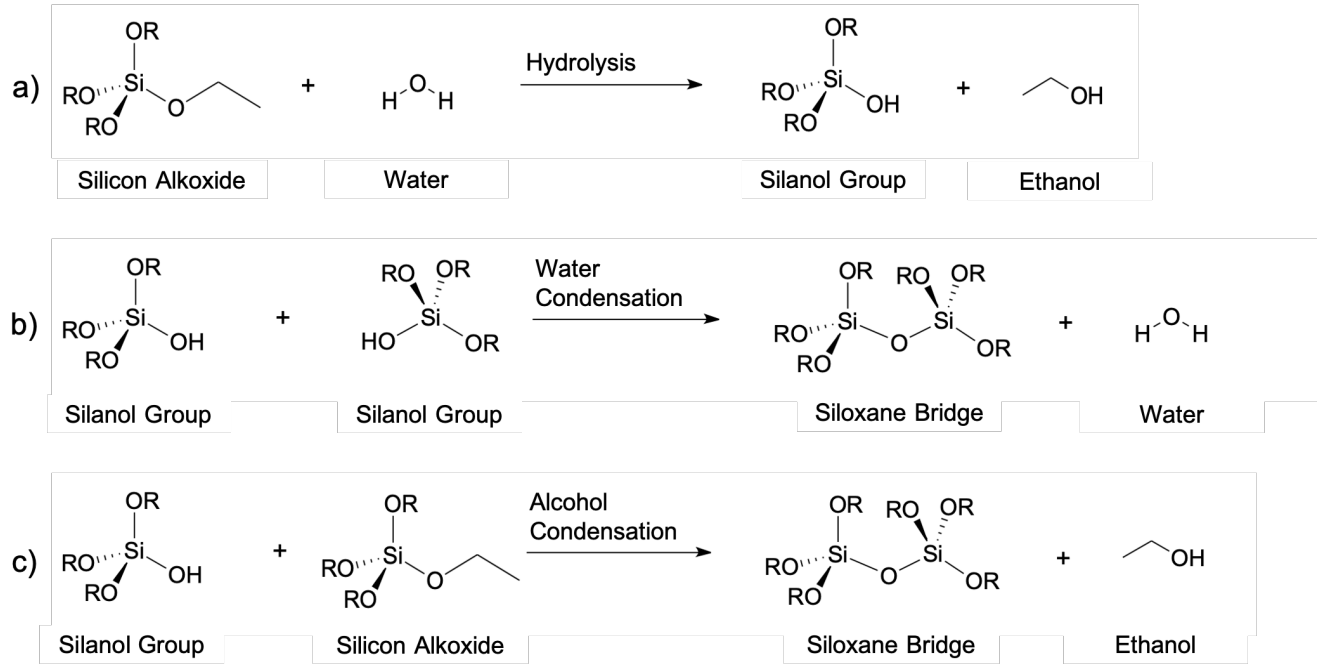


**Figure 2.1:** a) Hydrolysation reaction between TEOS and water. b) Condensation reaction between two hydrolysed TEOS (silanol groups) molecules and a water molecule splits off. c) Condensation reaction between hydrolysed TEOS (silanol groups) and TEOS, an ethanol molecule splits off. Structures are made in ChemDraw

### 2.3.2 Sol parameters and effects on coating structure

The structure and properties of the sol can be changed by adjusting the synthesis parameters. The structure can be varied by pH, solvent/TEOS ratio (S), $H_2O$/TEOS ratio (R) and type of solvent [36]. Different parameters will result in variations of functional groups (neighbour atom/group of silicon), chain length, branching and morphology [37].

The hydrolysis and condensation steps in the sol-gel process can be controlled by pH-adjusting the water added to initiate the hydrolysis reaction. For TEOS sols, the relative reaction rates for hydrolysis and condensation as a function of pH is shown in Figure 2.2.

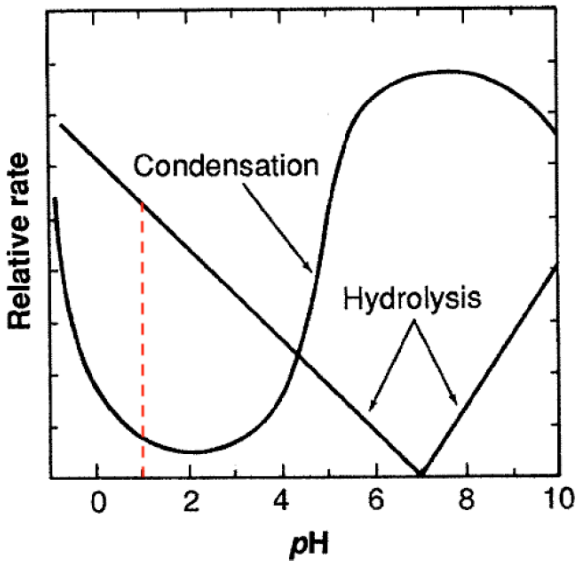


**Figure 2.2:** A schematic representation of hydrolysis and condensation rates in TEOS sols as a function pH. In this project the reaction is run at pH = 1. Modified from [36].

From the relative reaction rates in Figure 2.2 it can be found that hydrolysis is the dominating reaction when pH is below ∼4.5, and condensation reaction dominates for higher pH values. When the reaction is catalyzed by an acid, the acid will protonate the negatively charged alkoxide (OR') groups by $H_3O^+$-ions. The extent of hydrolyzed OR-groups is dependent on the amount of water added, the R-value. When a basic catalyst is used, the OR groups will be deprotonated and condensation is activated. Reactions between the nucleophiles and positively charged metal atoms will occur [36].

The structure in the final coating will differ when changing the pH of the catalyst. In acid-catalyzed sols, linear chained polymers will form, which result in a dense coating. This process is illustrated in Figure 2.3. By increasing the pH (condensation rate increases), a random aggregate formation will occur, leaving the final coating highly porous. For base-catalyzed sols, uniform particles will be formed (nano scale) leaving the final coating thick and less dense [38].

The molar ratio between alkoxide and water (R) will determine the extent of hydrolysis before the condensation takes place. For a coating system containing TEOS, EtOH and $H_2O$ the optimal R-value is 4 [39]. The extent of substitution of TEOS molecules will determine the sol morphology, if it is linear chains, rings or oligomers. The listed morphologies represent $H_2O$/TEOS molar ratios from low to high respectively [40].

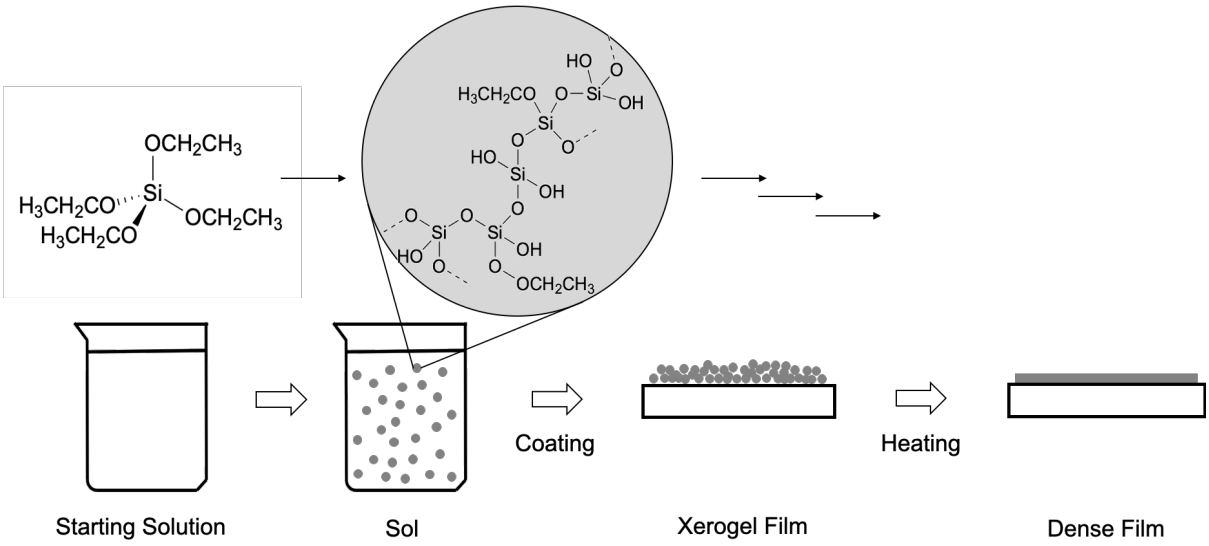


**Figure 2.3:** In an acidic catalysed sol gel synthesis, a long chained polymer will form and the deposited xerogel will turn into a dense coating after heat treatment and evaporation of solvent. The figure is modified from [38].

In the sol-gel process, the solvent is present to avoid phase separation when $H_2O$ is added to the precursor to initiate the hydrolysis step [36]. The miscible properties of the TEOS, $H_2O$ and EtOH system is found in the diagram in Figure 2.4

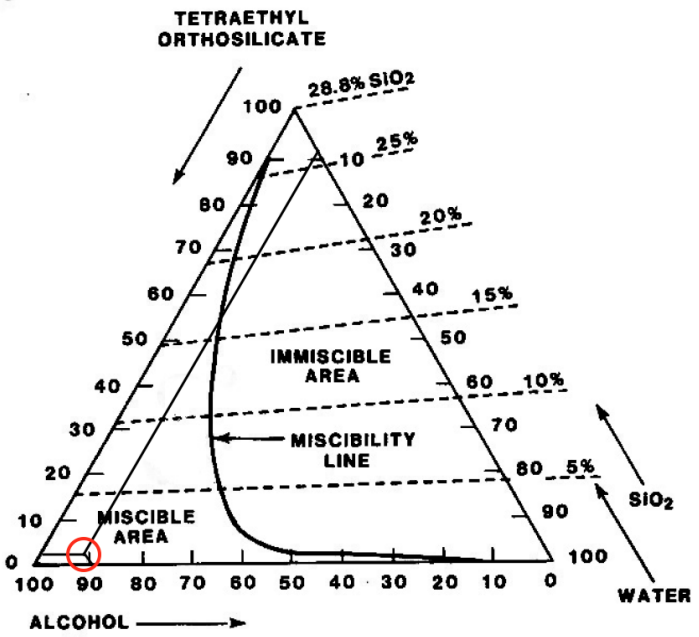


**Figure 2.4:** A ternary diagram for TEOS, $H_2O$ and EtOH showing the miscible and immiscible areas. The red circle indicate the phase composition for the sol in this project. Modified from [36].

## 2.4 Coatings Technology for Anti-Fouling Applications

This chapter provides strategies in coating technology for anti-fouling application and some important physical aspects on coating properties. Requirements for realization of coatings with anti-fouling properties are related to biological, chemical and physical factors. The chapter is partially adapted from previous work.

### 2.4.1 Anti-fouling and foul release paints

Biocidal anti-fouling (AF) paints are defined to contain one or more active ingredients (biocides) that control growth and settlement of fouling organisms on structures in the marine environment [41]. The effect is ensured by a more or less controlled biocidal release rate, into the surrounding environment (bulk sea water). The biocide can be left in a soluble or insoluble matrix, and the most common release mechanisms are contact leaching, soluble matrix and self polishing properties [42]. Contact leaching occurs in an insoluble matrix, and biocides are released from a thick leaching layer. In a soluble matrix, the biocides are released when the matrix dissolves. The self polishing mechanism reveals new narrow leaching layers when the matrix erodes.

Foul release (FR) coatings provides minimal adhesion of organisms to prevent attachment of marine biofilms. Coating requirements include a smooth and non-porous surface, free of reactive functional groups and low polarity. These factors facilitate for removal fouling settlements by water flow.

### 2.4.2 Hydrophilic surface characteristics and measurements

A solid surface is described as hydrophilic or hydrophopic, depending on water absorbing or water repellent properties during wetting. The wettability is often characterized by the contact angle, $\theta_c$, which is defined as the angle between the liquid-surface interface and liquid-gas interface [32]. A relationship between the equilibrium contact angle, $\theta_0$, and the inerfacial specific energy between the three phases, is established in Young's Equation 2.1. The equation assume a smooth and chemically homogeneous surface.

$$cos\theta_0 = \frac{\gamma_{SG} - \gamma_{SL}}{\gamma_{LG}} \tag{2.1}$$

In the equation $\gamma_{SG}$ is the interfacial energy between solid and gas phase. $\gamma_{SL}$ is the solid-liquid interfacial energy and $\gamma_{LG}$ is the interfacial energy between liquid and gas.

Examples on differences in contact angles for hydrophilic and hydrophobic surfaces is presented in Figure 2.1.

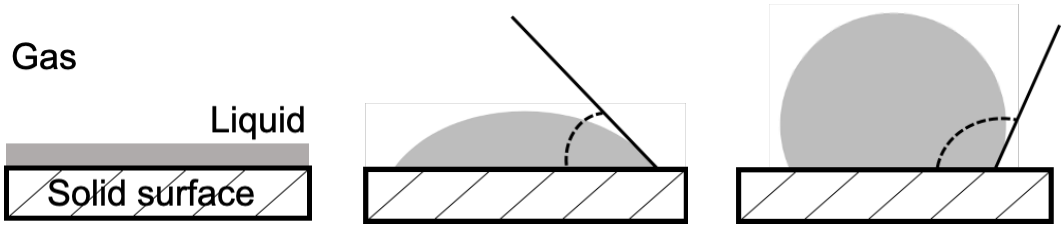


**(a)** Complete wetting, $\theta_c = 0°$ **(b)** Hydrophilic,$\theta_c < 90°$ **(c)** Hydrophobic, $\theta_c > 90°$

**Figure 2.1:** Drop shapes for a) a complete wetting, b) hydrophilic surface and c) hydrophobic surface. Phases are indicated in a)

From the figure it observed that lower contact angles are formed for surfaces with high wettability (large contact area between solid surface and liquid). In literature, hydrophilic surfaces are defined to have contact angles below 90° and hydrophobic surfaces have contact angles above 90° [32]. For water, hydrophilicity is the ability to form hydrogen bonds at the interface between solid and liquid phase [43]. The hydrophilic properties of a material are determined by chemical composition and microstructure [44].

Coatings with hydrophilic surfaces has raised as a new approach to avoid adhesion of biofilms on surfaces introduced to seawater. [45], and the anti-fouling performance is then determined by the hydrophilic character of the coating. The hydrophilicity is a limited property as it is reduced by wear and damages on the surface during operation, hence the durability of the anti-fouling functionality is reduced over time.

The microstructure is important to the wettability of for a given hydrophilic surface. By increasing the surface roughness, it can render more hydrophilic according to Wenzel's Equation 2.2 (and opposite for hydrophobic surfaces).

$$cos\theta_a = rcos\theta \tag{2.2}$$

where $\theta_a$ is the apparent contact angle on a rough surface and $\theta$ is the measured intrinsic contact angle on a planar surface. The r value represent the surface roughness and are defined as the ratio between actual surface area and the project surface area [44, 46]

### Contact angle measurements

An optical tensiometer is frequently used in determination of contact angels, surface tensions and interfacial tensions [47]. The sample is positions at a substrate table under a syringe tip with liquid phase. A camera is attached in sample heigh, focused on the sample

surface, to observe and record contact angles after drop deposition. Computer analysis software recognizes solid-liquid interface and fit the drop shape. A droplet volume of 1-10 $\mu$L is used for analysis. Larger volumes will cause uncertainties to the results regarding increased gravity influence. Dynamic contact angles show a significantly larger variations when larger droplet volumes are deposited, compared to static (initial) contact angles.

#### Atomic Force Microscopy (AFM) and surface topography

Profile characterization methods for surfaces can be categorized into contact or non-contact methods. In this work, Atomic force microscopy (AFM) was used in non-contact tapping mode, to study surface profile and topography. The surface data can be used to calculate the arithmetic surface roughness, $R_a$, which is the arithmetic mean of the absolute deviations of the roughness profile from the mean line for measured profile length. It is a universally recognized and standardized parameter for roughness [48]. $R_a$ is mathematically defined in Equation 2.3.

$$R_a = \frac{1}{n}\sum_{i=1}^{n} z_i \tag{2.3}$$

An atomic force microscope (AFM) is a scanning probe microscope and makes it possible to study surfaces at atomic levels. A probe is mounted to a piezoelectric ceramic material and cantilever, and placed by a few nanometers above the sample to be investigated. The piezoelectric element oscillates at a set amplitude close to free resonance and excites the cantilever [49]. The tip-to-sample distance is regulated by the resonance frequency and damping of the cantilever. When the distance to the surface decreases, the frequency of the cantilever increases due to repulsive forces acting on the tip, and the changes in frequencies are detected. Like this, the probe scans the surface, and the interactions (forces) between the probe tip and the sample surface, gives a topographic image of the surface [32].

### 2.4.3 Wear resistance of coatings

To reduce wear damage and further maintenance coast, a coating must proved good adhesive properties to the utilized construction material. [50]. The coating should adhere well in a wide range of temperatures and humidity conditions. The external conditions when applied should ideally not affect the performance of the coating. The adhesion strength and resistance to mechanical damage is an important factor for the durability of the coating. Erosion due to water movement is a particulate problem in shipping and vessels operating in high speed. The water line is most exposed to wear damage because of the continuously change in environment in this area. This area is repeatedly wet and dried and exposed to a higher variety of temperatures and light, and the breakdown of

the coatings in these regions are accelerated. [50].

#### Coating scratch tests

Instrumented scratch testing is a quantitative method for monitoring adhesion strength. The method increases reproducibility, sensitivity, and quantification in examination of scratch resistance of coatings [51].

Scratch testers provides a constant or progressive normal force, while the mounted sample is dragged across a diamond-tipped stylus. Scratch testers can also monitor penetration depth, lateral friction force, and acoustic emission. Constitution of coating failure depends on the application, and the scratch tolerance is dependent on coating purpose. Cohesive coating failures deform the coating and may affect finish sheen. In protective coatings, cohesive damage may fit within the tolerances of the performance. Adhesive failure involves rupture and loss of material contact. Subsequent the substrate material is exposed. Adhesive coating failures are normally quickly followed by loss of function.

### 2.4.4 Coating deposition techniques

There are several methods used for coating deposition, where techniques as spray, dip and spin coating are commonly used. Coating for anti-fouling applications are usually sprayed on to the surface, due to the large constructions and surface areas.

Spray coating provides a technique for coating of large and complex constructions. Hand held spray coating might cause an uneven surface due to less control of motion and number of layers. Variables that will affect the final coated surface is the working distance, temperature, pressure (from the propulsion gas) and drop size [52].

## 2.5 Graphene Oxide as Antibacterial Agent

This chapter suggests mechanisms for antibacterial activity of graphene oxide. The presented research was chosen due to similar topic and relevance for this thesis.

### 2.5.1 Antibacterial mechanisms in graphene oxide

From several studies, GMs are proved to exhibit growth inhibiting properties of microorganisms [53, 54, 55]. The physiochemical interactions between GO and microorganisms are thought to determine the antibacterial activity, where GO size, concentration, morphology, exposure time and type of microbes are factors that influence the GO antibacterial interactions [8, 56].

There are mainly three possible mechanisms that are believed to describe the antibacterial behavior of GO. The first one is due to material morphology, and sharp edges in GO nanosheets, referred to as nanoknives. The sharp edges cut through the phospholipidic layer in the cell membrane, and causes cell disruption. Another mechanism is oxidative stress and the production of reduced oxygen species (ROS) within an organism, by damaging the cell membrane. The last theory is wrapping or trapping of bacteria by flexible GO thin films, and limits the the access to key resources (space, nutrients) [57].

### 2.5.2 Relevant methodology and results

Liu et al. [53] prepared GO coatings on polymer substrate, and the antibacterial activity against the bacteria *E.coli* and *S.aerus* was investigated. The results from the experiments showed that growth of E.coli was more inhibited compared to *S.aerus*. This confirms the biological factor dependency on biofilm formation, and that individual species has its unique biology and susceptibility to biocides. In the work, GO was coated parallel to the substrate, leaving the coating smooth and without sharp edges. This eliminated the sharp edges of GO to cause cell rupture, and oxidative stress was the considered factor of anti-fouling activity. A number of studies report the stress-induced toxicity properties of graphene oxide to explain the antibacterial activity in the material [53, 54].

### 2.5.3 Comments on toxic effects

Graphene oxide exhibit low cytotoxity, compared to its counterpart (rGO exhibit the highest cytotoxicity), and are found to have the strongest antibacterial activity among the GMs due to extent of oxygen groups [58, 59]. There are little research available on the long term effects of GO and possible accumulations in the marine environment and its species.

# 3 Experimental

The flow chart in Figure 3.1 provides a schematic overview of the experimental work preformed in this Masters's Thesis. In the following chapter, detailed information on each of the executed steps are presented. All details regarding characterization methods and instrumental settings are included in the chapter.

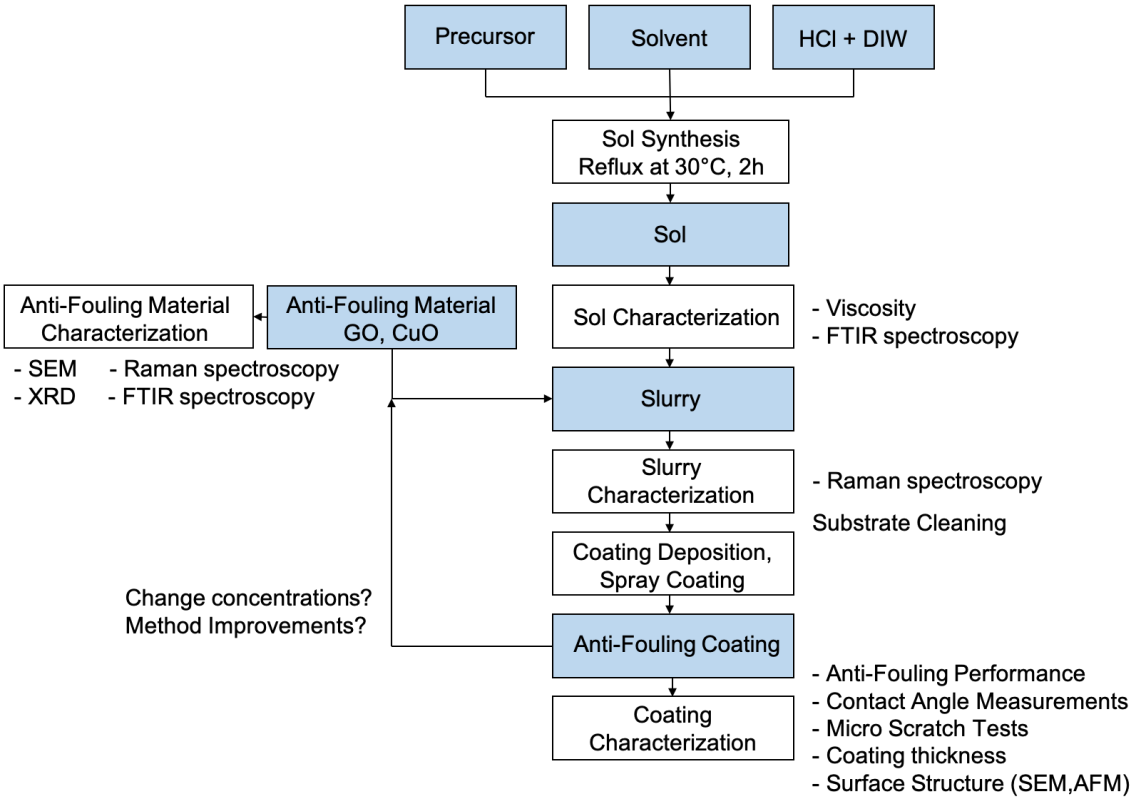


**Figure 3.1:** Overview of the experimental work preformed in the Master's thesis.

The experimental work is partly adapted from previous projects at the Department of Material Science and Engineering at the Norwegian University of Science and Technology (NTNU) [10, 60]. The methods are based on scientific papers addressing similar experimental work, and empirical research.

## 3.1 Preparation of Silica Sol

### 3.1.1 Chemicals

The silica-based sol was synthesized from the chemicals listed in Table 3.1.

**Table 3.1:** Chemicals used in synthesis of silica sol.

| Chemical | Formula | Supplier | CAS no. | Function |
|---|---|---|---|---|
| Tetraethyl orthosilicate (98%) | $SiC_8H_{20}O_4$ | Sigma Aldrich | 78-10-4 | Precursor |
| Ethanol (99.97%) | $C_2H_5OH$ | VWR | 64-17-5 | Solvent |
| Hydrochloric acid (32%) | HCl | VWR | 7647-01-0 | Catalyst |
| Deionized water | $H_2O$ | | 7732-18-5 | |

The properties of the chemicals and molar ratio used for the synthesis, are given in Table 3.2.

**Table 3.2:** Chemicals used in synthesis of silica sol.

| Chemical | Abbrevation | $M_m$ [g/mol] | $\rho$ [g/mL] | Molar ratio |
|---|---|---|---|---|
| Tetraethyl orthosilicate (98%) | TEOS | 208.33 | 0.933 | 1 |
| Ethanol (99.97%) | EtOH | 46.07 | 0.790 | 36.8 |
| Hydrochloric acid (32%) | HCl | 36.46 | 1.180 | 0.01 |
| Deionized water | DIW | 18.02 | 0.998 | 4 |

The molar ratios are adapted from the procedure suggested by Ye et al. [44]. The method was chosen due to the high molar ratio of solvent (EtOH), with purpose to stabilize (dilute) the dispersion when adding GO and CuO. In Table 3.3 the chemical volumes in 100 mL sol is presented. The equations used for calculations are derived in Appendix A. Chemicals were measured with micropipettes providing a three decimal precision.

**Table 3.3:** Volumes of chemical compounds used for synthesis of 100 mL silica sol.

| Chemical | Purity | $n$ [mol] | $V$ [mL] |
|---|---|---|---|
| TEOS | 98% | 0.0408 | 9.303 |
| EtOH | 99.97% | 1.503 | 87.708 |
| HCl | 32% | 0.000408 | 0.039 |
| DIW | 100% | 0.163 | 2.949 |

### 3.1.2 Procedure

The sol was prepared by mixing precursor and solvent, before adding pH-adjusted water (pH = 1) drop wise from a burette to the solution, under constant stirring of 600 rpm. The chemicals were mixed in a 250 mL round-bottom flask in a water bath with a condenser attached. The sol was immediately stirred for 2 hours at 30°C under reflux, to avoid evaporation of solvent. The experimental setup is shown in Figure 3.1. The prepared sol was cooled to room temperature and stored in glass containers at 6°C.

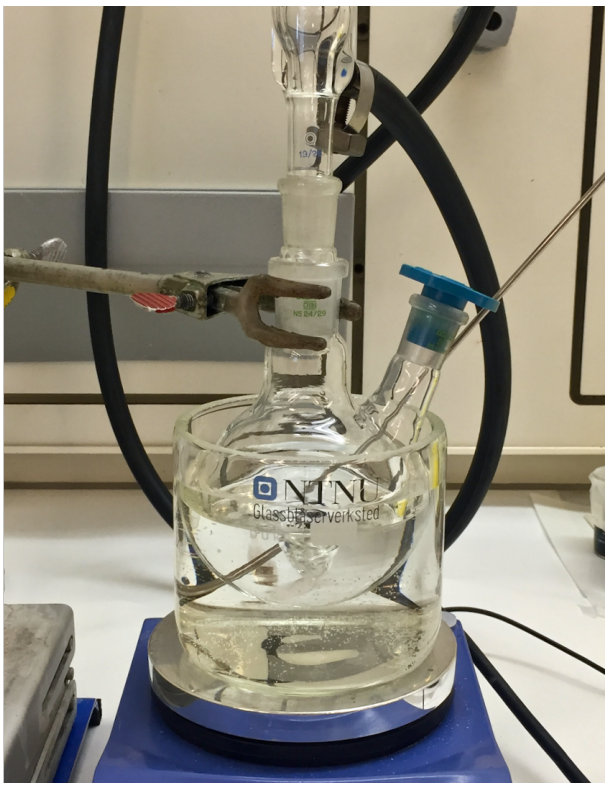


**Figure 3.1:** The experimental setup for the sol synthesis. The sol was heated at 30 °C for 2 h under reflux and constant stirring (600 rpm).

**Laboratory Equipment**

Micropipettes, burette, round-bottom flask (250 mL), reflux condenser, crystallization disc, heating element with thermometer, magnet, magnetic stirrer, stand with clamps, pH indicator strips (for low pH values).

## 3.2 Sol characterization

### 3.2.1 Rheometry

Rheological properties and sol ageing was characterized by viscosity measurements. The viscosity values were measured by *HAAKE MARS III Modular Advanced Rheometer*

*System* (Thermo Scientific) with measuring geometry CC27 DG Ti Cylinder double-gap. The geometry is suitable for low viscosity measurements at constant temperatures. The measurements were preformed at 20° C in normal atmosphere. Each measurement required 1.85 mL solution. The flow behaviour was measured in constant shear rate (CR) mode by the program given in Table 3.1.

**Table 3.1:** Operating parameters in the viscosity measurements of the sol.

| Program | Shear rate [1/s] | Time [s] | Temperature [°C] |
|---|---|---|---|
| 1 | 0.0010 - 500.0 | 180 | 20 |
| 2 | 500.0 | 30 | 20 |
| 3 | 500.0 - 0.0010 | 180 | 20 |

The viscosity was measured <1, 24 and 48 hours after sol synthesis.

### 3.2.2 FTIR spectroscopy

FTIR spectroscopy was used to investigate and confirm functional groups in the sol. A *Bruker vertex 80V* FTIR spectrometer was used. Spectra were obtained in transmission mode using an attenuated total reflection (ATR) test technique. Data was saved in range from 350-4000 $cm^{-1}$ (mid-infrared) and sample scan time was set to 124 scans. A background scan was run in the beginning of each session, in order to remove signals from external environment. The samples were deposited to the ATR crystal using a pipette and dried before the sample compartment was evacuated.

## 3.3 Material Characterization

Graphene oxide and copper(II)oxide were used as anti-fouling materials in the prepared coatings, and the materials were initially characterized by SEM imaging and X-ray diffraction (XRD) analysis. GO was additionally studied by FTIR and Raman spectroscopy to characterize the oxidation state and chemical bonds in the material. The coating slurries were also characterized by Raman spectroscopy to investigate structural changes in GO when added to the silica sol. The FTIR apparatus settings were the same as for sol characterization.

Field emission scanning electron microscopy (SEM) with detector Zeiss Supra 55 SE, was used to look at material characteristics, coated surface structures and cross sections of the coatings. The working distance was set at ∼6 mm and the accelerating voltage was 5 kV. The low accelerating voltage ensured imaging on the surface due to low emission volume.

### 3.3.1 XRD analysis

X-ray diffraction was used to classify the crystallographic character and phases in the provided materials. Copper(II)oxide nanopowder was prepared by packing the powder in a sample mould and cover it with kapton film, to keep the powder in place. The sample was scanned in an X-Ray Diffractometer, *D8 A25 Da Vinci* with scan time 1 hour and scanning detector angle ($2\theta$) ranging from 20° to 80°. The graphene oxide sample was prepared by applying dispersed GO paste (in water), dropwise to a silicon (Si) plate. The sample was dried before scanning. Scan time was 1 hour with $2\theta$ going from 5 to 75°. The prepared samples are imaged in Figure 3.1

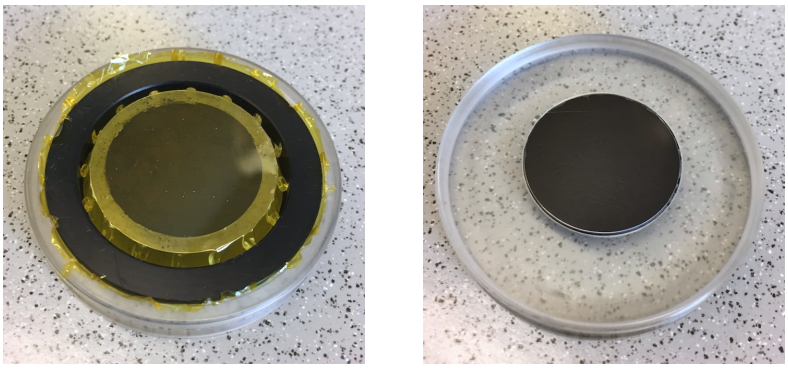

**(a)** Copper(II)oxide sample **(b)** Graphene oxide sample

**Figure 3.1:** X-Ray Diffraction sample preparation of a) CuO and b) GO.

### 3.3.2 Raman spectroscopy

Raman spectroscopy was used to identify the carbon bonds (originally from graphene) in GO paste and GO slurries. A *WITech alpha300 R*, confocal Raman imaging microscope with a green laser (532 nm) was used to obtain the spectra. The instrument was calibrated with a silicon plate before use. Laser voltage was kept low to avoid burns in the samples, and was set to 5V.

One drop of sample was applied to a plate of glass, dried, and placed under the optical light microscope (50X) in bright field mode. A large area Raman map was made for the sample, using the image stitching function. The final spectrum represent an average of ten single spectra at random positions, where the sample surface is focused in the OM. Background and cosmic rays were removed from each single spectrum before calculating the average. To reveal hidden peaks and obtain true peak intensity for Raman shifts, the curves were deconvoluted and fitted. The software Fityk (version 1.3.1) was used to deconvolute Raman peaks by identification of Lorenzian and Gaussian functions.

## 3.4 Incorporating Anti-Fouling Material to Sol

### 3.4.1 Preparation of graphene oxide stock solution

A GO stock solution was made by mixing GO paste (10 wt% GO) and EtOH (99.97%, VWR) to wanted concentration of 2.0 mg GO/mL solution. 1.001 g of GO paste was mixed with ∼20 mL of EtOH and stirred manually until GO was dispersed. The dispersion was diluted to 50 mL in a volumetric flask and stirred at 600 rpm for 30 min. The dispersion was sonicated for 2 minutes.

**Laboratory Equipment**
Beaker, spatula, micro scale weight, volumetric flask, magnetic stirrer, magnet, ultrasonic bath.

### 3.4.2 Slurry preparation

GO stock solution was added to the sol in different volumes. The weight ratios between TEOS and GO in the slurries are given in Table 3.1, including the volumes of each component.

**Table 3.1:** Mixed volumes of silica sol and GO stock solution in slurries. GO/TEOS represent the weight ratio between the components.

| Coating ID | $V_{sol}$ [mL] | $V_{GO}$ [mL] | GO/TEOS |
|---|---|---|---|
| C-Ref | 10 | 0 | 0 |
| GO C-100 | 10 | 4.253 | 0.0100 |
| GO C-125 | 10 | 5.317 | 0.00125 |
| GO C-150 | 10 | 6.380 | 0.0150 |

CuO nanopowder was added to the sol in the same weight ratios as for the graphene oxide coating. The masses added are shown in Table 3.2. There was assumed no change in volume.

**Table 3.2:** The amounts of silica sol and CuO NPs in the slurries. CuO/TEOS represent the weight ratio between the two components.

| Coating ID | $V_{sol}$ [mL] | $m_{CuO}$ [g] | CuO/TEOS |
|---|---|---|---|
| CuO C-100 | 10 | 0.0085 | 0.00100 |
| CuO C-125 | 10 | 0.0106 | 0.00125 |
| CuO C-150 | 10 | 0.0128 | 0.0150 |

The CuO slurries were sonicated for 10 min in ultrasonic bath before spray coated on substrates. This to ensure well dispersed particles in the coated layer.

### 3.4.3 Coating preparation

#### Substrate cleaning

Figure 3.1 provides images of the substrates used in this work. Polyethylene substrates were cut to measure the sample holders in the biofilm reactor. 316 steel (mill finish) samples measured 1 cm · 2 cm. Both substrates were customized at the fine mechanical workshop at NTNU. The substrates were prepared for coating deposition by the routes explained in Table 3.3. The substrates were left in the solvents until right before use, and carefully dried with cleanroom wipes before coated.

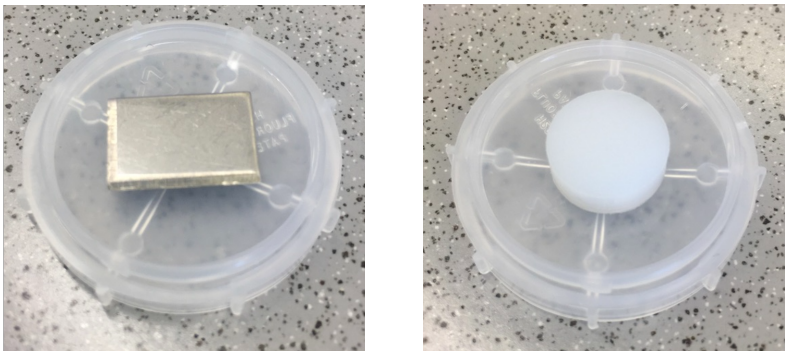

**(a)** 316 Steel Substrate **(b)** Polyethylene Substrate

**Figure 3.1:** Images of substrates a) 316 steel and b) PE, both customized for the purpose in this work at the fine mechanical workshop at NTNU.

**Table 3.3:** Substrate cleaning procedure

| Substrate | Chemicals | Method |
|---|---|---|
| 316 Stainless Steel | Acetone, Isopropanol | The substrates were washed in acetone for 10 minutes (ultrasonic bath) then left in isopropanol. |
| PE | Ethanol | The substrates were washed in ethanol for 10 minutes (ultrasonic bath). |

#### Spray coating parameters

The slurries were sprayed on the substrates by a hand-held airbrush. The pressure was set to 2 bar with nitrogen as propulsion gas, the working distance was ∼7 cm, and the spraying angle 90° to the surface. The substrates were coated in 1-5 layers.

#### Heat treatment

The coated substrates were dried in room temperature and heated in a *Carbolite Gero* oven for sol gel, at 60° C for 6 h. The step was preformed to remove excess solvent.

## 3.5 Coating Characterization Methods

### 3.5.1 Cross sectional analysis

Coated steel samples were cast in epoxy and manually ground approximately 1/3 of its height by 280 SiC paper using a *Strues LaboPol-21* spinning disk (300 rpm). The samples were then polished on a 800 SiC paper until the sample surface appeared flat. The samples were then transferred to an automatic polisher, *Struers Tegramin-20*. The polishing program is provided in Table 3.1. Between each step of grounding and polishing, the samples were carefully cleaned in water and ethanol to remove dust and particles. The coating cross section was examined in SEM and by element analysis, EDS.

**Table 3.1:** Coating sample polishing program.

| Step | Surface disk | Suspension | Time [min] |
|---|---|---|---|
| 1 | Plan | DiaPro, Plan9 (9$\mu$m) | 2 |
| 2 | Nap | DiaPro, Nap-B1 (1$\mu$m) | 2 |

### 3.5.2 Surface profile and topography

Roughness and surface profile data were obtained by atomic force microscopy (AFM) using an *Agilent Technologies 5500 AFM* in tapping mode, with dynamic force and scanning area 10$\mu$m $\cdot$ 10$\mu$m. Tap300Al-G, aluminium coated silicon AFM probes for tapping mode and intermittent contact were used.

### 3.5.3 Micro scratch tests

Coating adhesion strength and wear resistance were measured by a micro scratch tests in an *Anton Paar Micro Scratch Tester*. The scratch tester generates a controlled scratch by applying load to a diamond tip (100m radius), positioned on the very surface of the sample. The scratches made measured 3 mm, and a progressive load was applied. Initial load was set to 30 mN and final load to 10,000 mN. Pre- and postscans were preformed to find the initial surface profile and coating recovery. Recovery was measured 180 s after the scratch test. A detailed overview of the scratch program is given in Table 3.2

**Table 3.2:** A three step micro scratch test program for adhesion strength and coating recovery.

| Step | Load [mN] | Length [mm] | Hold [s] |
|---|---|---|---|
| 1 | 30 | 3 | 0 |
| 2 | 30-10,000 | 3 | 180 |
| 3 | 30 | 3 | 0 |

The scratches were assessed by the optical microscope connected to the instrument, and studied at 5X magnification.

### 3.5.4 Contact angle measurements

The coated steel substrates were tested for hydrophilic properties by contact angle measurements. The contact angles were measured by a *Krüss Drop Shape Analyser*. Sessile drop mode was used as the measuring method and Ellipse (Tangent-1) set as fitting model. The baseline was set automatically. The water drop volume measured 1.6 L and the flow rate was 0.3 $\mu$L/s. Contact angles were automatically recorded 0.5 seconds after water deposition. All measurements were preformed in room temperature.

## 3.6 Biofilm Production

The growth inhibiting coating properties were tested in a biofilm reactor. The biofilm reactor and experimental setup are shown in Figure 3.1. The coated PE substrates were mounted to sample holders in the reactor and covered with seawater. A water flow rate of 5 L/min ensured equal distribution of organisms within the reactor. The temperature conditions outside the reactor were kept constant by placing the reactor in a water bath with a constant temperature of 15°C. Both a cooler and a heating element ensured constant temperature, controlled by a thermostat in the control unit. The water bath was covered with plastic water bath balls for insulation and vapour control.

Five different growth experiments were run, with variations in anti-fouling material, time and addition of nutrients. Gulliard's f/2 medium with Si was used as enriched seawater medium. In the experiments with added nutrients, 16 mL f/2 was initially added to 800 mL of seawater (mixing ratio 0.02:1). A detailed overview of the variables are presented in Table 3.1. The rest of the parameters were kept constant (temperature, flow rate and light access).

In experiment 1 in Table 3.1, samples were extracted after 7, 14 and 28 days from the same batch, to study the growth of bacteria over time. Experiment 2-5 compared growth inhibiting effects for the anti-fouling materials, with and without additions of nutrients.

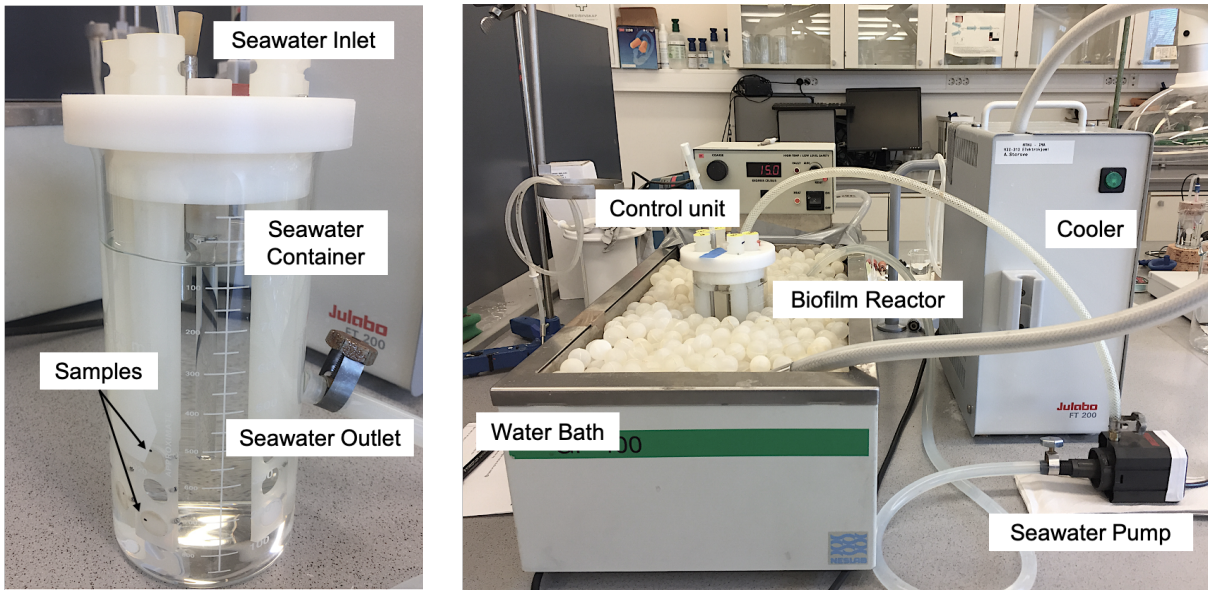


**(a)** Biofilm reactor **(b)** Experimental setup

**Figure 3.1:** The a) biofilm reactor sample compartment and b) experimental setup including the biofilm reactor. The prepared reactor with seawater flow and mounted samples was submerged in a water bath. Seawater was pumped continuously through the reactor, and circulated through the water pump and plastic tubes. The temperature was kept constant by a thermostat in the control unit and attached cooler and heating element.

**Table 3.1:** Experimental Details on Biofilm Growth.

| Experiment no. | Anti-Fouling Agent | Time [days] | f/2 medium |
|---|---|---|---|
| 1 | Graphene Oxide | 7, 14, 28 | Yes |
| 2 | Graphene Oxide | 7 | No |
| 3 | Graphene Oxide | 7 | Yes |
| 4 | Copper Oxide | 7 | No |
| 5 | Copper Oxide | 7 | Yes |

### 3.6.1 Biofilm Characterization

The produced biofilms were studied and characterized in SEM. Before imaging, the substrates were sputtered with gold nanoparticles for 1 minute in an *Edwards Sputter Coater S150B*. Conducting tape ensured conductivity between sample surface and SEM stage and reduced charging. The SEM apparatus settings used are presented in previous Section (2.2).

# 4 Results

This chapter is divided into subsections based on the performed steps of synthesis and characterization presented in Figure 3.1.

## 4.1 Material Characterization

The studied anti-fouling materials were provided from suppliers, and a qualitative characterization was initially preformed. Both the graphene oxide paste (10wt% aqueous GO) and copper(II)oxide (nanopowder) were characterized. In graphene materials there are found large variations in functionalization and extent of oxygen groups. Hence, GO was thoroughly studied. CealTech AS provided a TEM and EDS analysis on the GO material, and these results are given in Appendix B.

### 4.1.1 SEM imaging

SEM images of graphene oxide and copper oxide are provided in Figure 4.1.

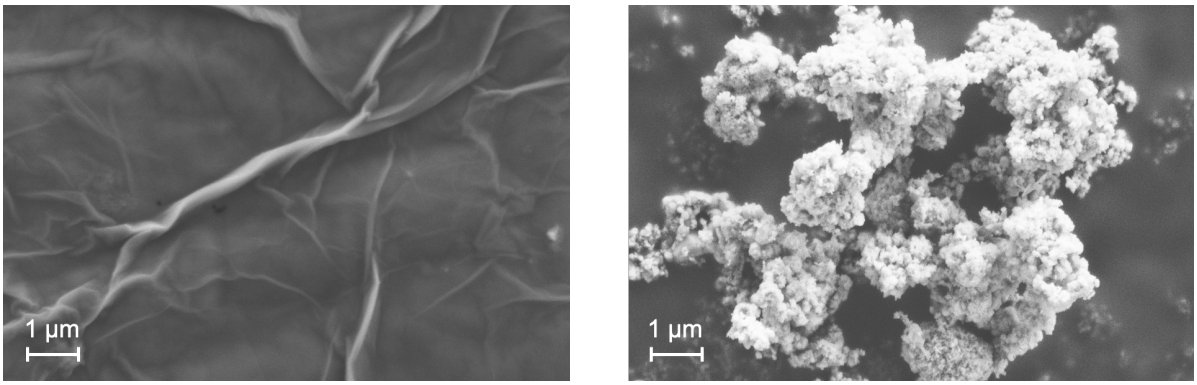


**(a)** Graphene Oxide **(b)** Copper Oxide

**Figure 4.1:** SEM images of a) graphene oxide nano sheets and b) agglomerates of copper oxide nanoparticles. Diluted dispersions of particles in water was applied to SEM stub and samples were dried before characterization.

The SEM image of GO visualizes the characteristic wrinkled structure formed by folds in the GO nano sheets. The powder sample of CuO show agglomerated powder particles. Single sheet- or particle sizes were not possible to determine from the SEM images with the utilized sample preparation method.

### 4.1.2 X-ray diffraction

The XRD patterns of GO and CuO samples are displayed in Figure 4.2 and 4.3 respectively, including the Miller indices. From the assessment of Bragg reflections for GO, an intense crystalline peak was found at $2\theta = 11.9$ corresponding to the (001) lattice plane [61, 62]. The sharp and distinct peak in the diffractogram is attributed to the preserved (from pure graphene) and ordered stacking along the c-axis. During oxidation the interlayer spacing increases (compared to graphene), due to introduced water, and the presence of oxygen groups which populate on the basal plane of the carbon sheet [63, 64].

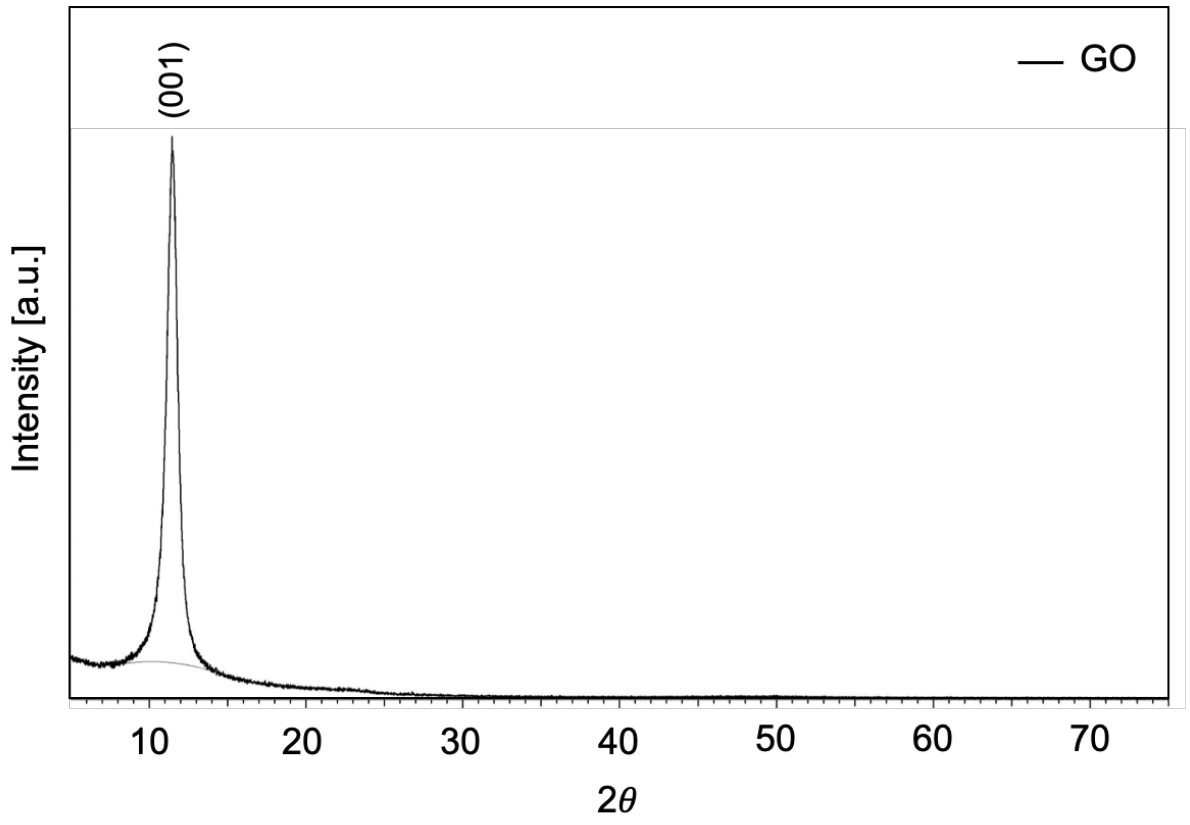


**Figure 4.2:** XRD pattern of GO sample with lattice plane (001) at $2\theta = 11.9°$.

All the Bragg reflections from the CuO nanoparticles sample can be assigned to the indexed diffraction lines of CuO tenorite [65, 66]. The highest diffraction intensity for copper oxide is observed from the (002) lattice plane at $2\theta = 36.7$.

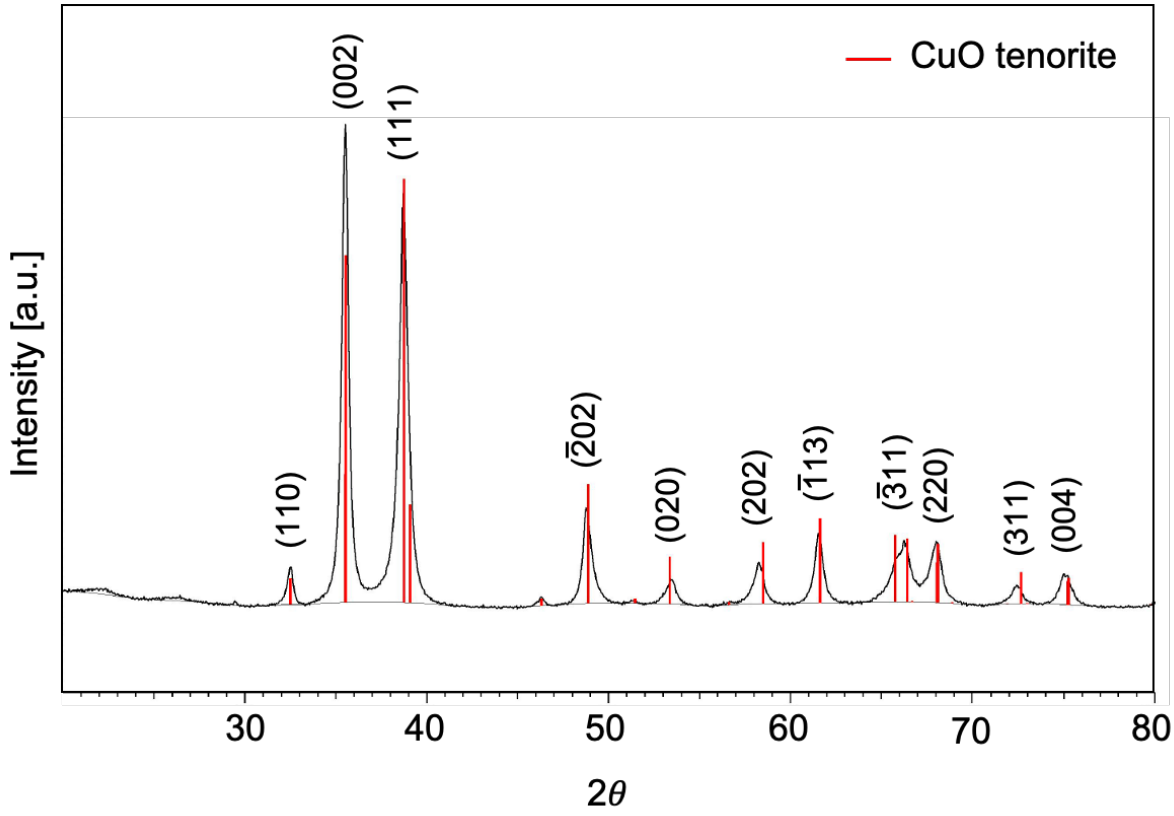


**Figure 4.3:** XRD pattern of CuO nanoparticles sample with Miller indices for CuO lattice planes. The highest diffraction intensity for CuO is observed from the $(\bar{1}11)$ lattice plane at $2\theta = 36.7°$. The Bragg reflections from the CuO sample can be assigned to the indexed diffraction lines for CuO tenorite (red lines, COD ID 1011194 [65]).

### 4.1.3 Raman spectra

The determination of carbon bands and disorder in the GO structure was obtained from the average Raman spectrum (origins from ten spectra) in Figure 4.4. The figure shows the deconvolution of the observed D and G bands from raw data. The plot proposes a deconvolution of the D, G, D', D*, D**, 2D, and G+D bands. The high presence and variation of D peaks attributes to a highly disordered GO structure due to oxygen functionalities formed during oxidation of graphene. The considerable presence of oxygen groups is confirmed from the elemental analysis provided in A.2.

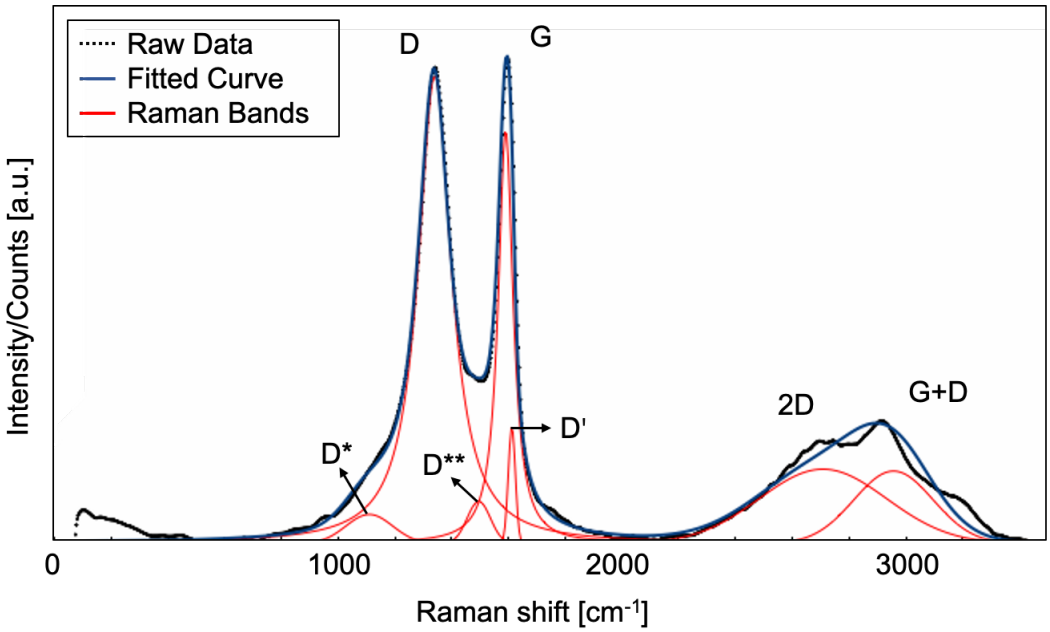


**Figure 4.4:** Raman spectrum of graphene oxide with proposed deconvolution of D, G, D', D*, D**, 2D, and D + G bands. GO has a highly disordered structure due to many functional groups formed during oxidation of graphene. The position of the D band is 1340 $cm^{-1}$ and of the G band is 1590 $cm^{-1}$. The $I_D$ /$I_G$ ratio is 1.13

The D and G peak is of interest as the ratio between them gives information about extent of oxidation and further the reactivity in the material. The peak positions, peak intensities and intensity ratio are presented in Table 4.1. The D and G peak positions, at respectively 1340 $cm^{-1}$ and 1590 $cm^{-1}$, are in good agreement with literature [67].

**Table 4.1:** Peak values for D and G bands in 10wt% GO in water. Values are adapted from Figure 4.4

| 10 wt% GO | D Band | G Band |
|---|---|---|
| Peak Position, P [1/cm] | 1340 | 1590 |
| Peak Intensity, I [CCD cts] | 7253 | 6424 |
| Intensity ratio, $I_D/I_G$ | 1.13 | |

A peak intensity ratio, between D and G peaks, above 1 tells that $sp^3$ bonded carbon is the dominating bond in the carbon structure (diamond structure). The oxidization is not complete, as there still is $sp^2$ bonded carbon (graphite structure), present from the observed G band.

### 4.1.4 FTIR spectrum

The structural groups in graphene oxide were characterized by FTIR spectroscopy and the provided spectrum is given in Figure 4.5.

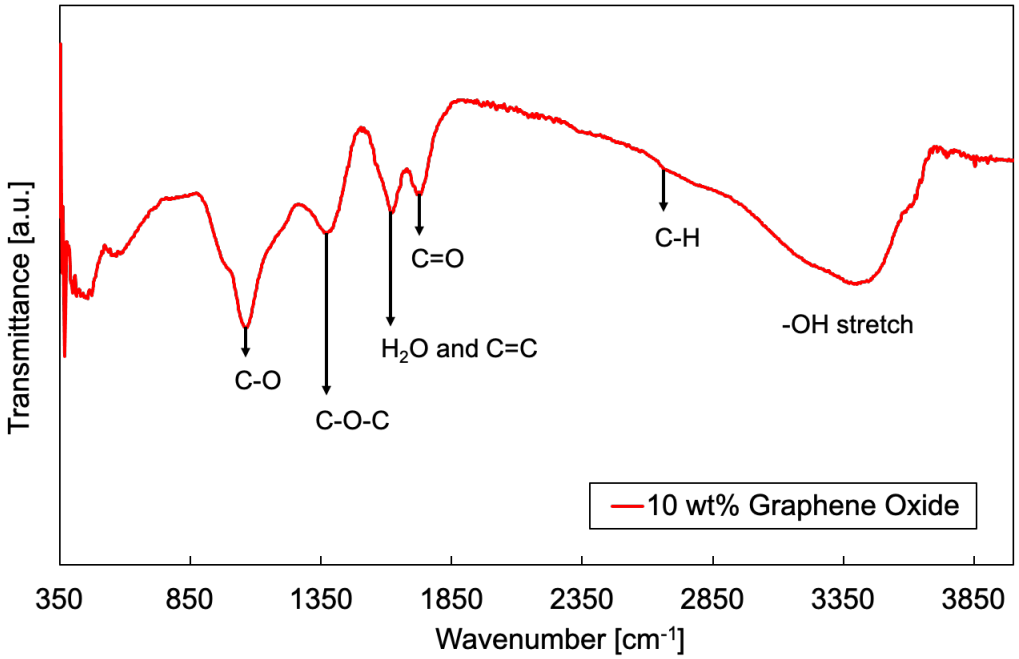


**Figure 4.5:** FTIR (ATR, attenuated total reflectance) spectrum of graphene oxide with a proposed assignment of structural groups for the most notable peak values.

From the observed peaks in Figure 4.5, a proposed assignment of structural groups present in GO is made. The broad peak from 2800-3600 $cm^{-1}$ attributed to water and hydroxyl groups ($H_2O$ and O-H). Usually ~3200-3500 $cm^{-1}$ is called the O-H stretch, and the large broadening of the peak indicates the presence of carboxylic acids (-COOH) in the material. At 2725 $cm^{-1}$ the C-H bonds are found. Other peaks observed in the spectrum show that GO is rich in carboxyl groups (C=O) with the visible peak around 1733 $cm^{-1}$. Epoxy groups (C-O-C) has the 1381 $cm^{-1}$ peak. The 1624 $cm^{-1}$ peak indicate the presence of liquid water, but can also origin from carbon double bonds (C=C) present in graphitic carbon (graphene). The peak at 1076 $cm^{-}1$ is assigned to hydroxyl groups (C-O). The frequency bands are in good agreement with analysis of spectrum acquired for similar material by Jaworski et al. [67].

## 4.2 Sol Characterization

The sol synthesis presented in this thesis has been tested in previous projects and are found to work well for the purpose of this work. The sol reactions, hydrolysis and condensation of alkoxide and silanol, and siloxane structures were studied by rheological analysis and FTIR spectroscopy. In the following section the sol characteristics will be presented.

### 4.2.1 Rheological properties

The viscosity values $\mu$ were calculated from the average viscosity as a function of shear rate (0.0010-500.0 $s^{-1}$, only for increasing shear rates). Outliers caused by instrumental errors were removed from the raw data set. The viscosity values were measured <1 ($\eta_0$), 24 ($\eta_{24}$) and 48($\eta_{48}$) hours after synthesis, and are found to be $\eta_0$ = 0.0022 Pa·s and $\eta_{24} = \eta_{48}$ = 0.0024 Pa·s. The values are presented in Figure 4.1 and represent the slope between the plotted shear stress and shear rate. The results show that the viscosity increases slightly after 24 hours, but is assumed to be constant as a function of time. From visual observations there was no change in appearance (gelation, phase separation or precipitation) of the sol over time. The sol is imaged in Figure 4.2.

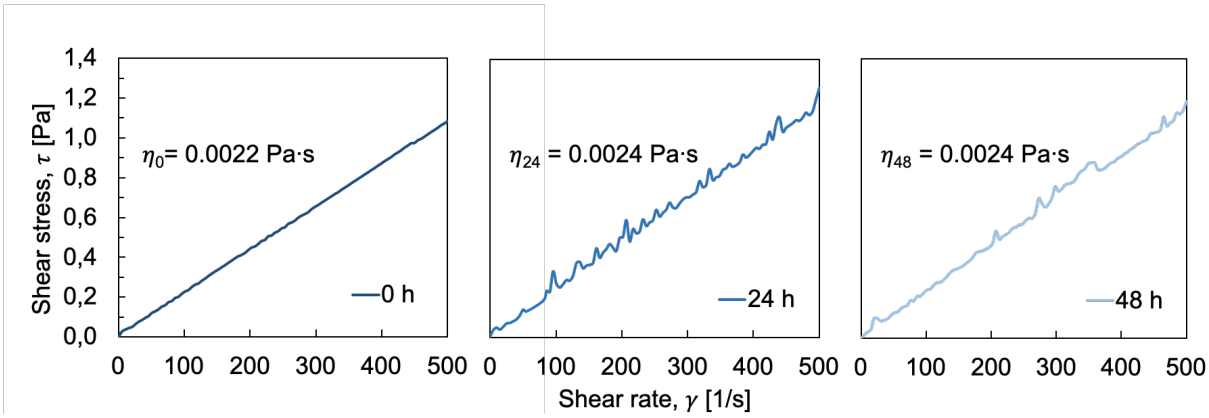


**Figure 4.1:** From the calculated viscosity values ($\eta$) the sol is assumed to be constant for all times measured. The sol exhibits Newtonian behaviour at all times analysed.

By examining the plotted data in Figure 4.1, it is evident that the shear stress arising from the flow behaviour is linearly dependent on the shear rate, and the sol exhibits Newtoninan behaviour.

**Figure 4.2:** Caption of synthesized silica sol. No change in visual appearance was observed over time.

### 4.2.2 FTIR spectra

The hydrolysis and condensation reaction was further characterized by FTIR spectroscopy to be able to relate the synthesis parameters to the sol structure, and the results are shown in Figure 4.3. The assignment of frequency bands detected for the sol were compared to Ye et. al. [44]. The performed FTIR analysis was in good agreement with literature, and is assumed to be a reliable detection method for the silica sol. The time dependent difference in peak intensities indicate that the hydrolysis and condensation reactions continue after 2 hours of synthesis.

From the observed frequency bands in the FTIR spectra, a proposed assignment of structural groups was made. The frequency band ranging from 3000cm$^{-1}$ to 3500 cm$^{-1}$ represent the hydroxide groups and water (-OH stretch and $H_2O$). There are two transmittance peaks at 2950 cm$^{-1}$ and 2985 cm$^{-1}$ corresponding to the C-H stretching vibration. The peak at 1132 cm$^{-1}$ corresponds to the C-H bending vibration. Peaks in the fingerprint area (350-1350 cm$^{-1}$) are typical bands of silica from sol-gel process. The peak at 1040 cm$^{-1}$ origins from Si-O-Si stretching, and Si-O-C stretching band is found at 920 cm$^{-1}$. The 784 cm$^{-1}$ peak is assigned to Si-O symmetric stretch. Asymmetric bending vibrations of Si-O and Si-O-Si are found at the frequency bands 607 cm$^{-1}$ and 413 cm$^{-1}$ respectively.

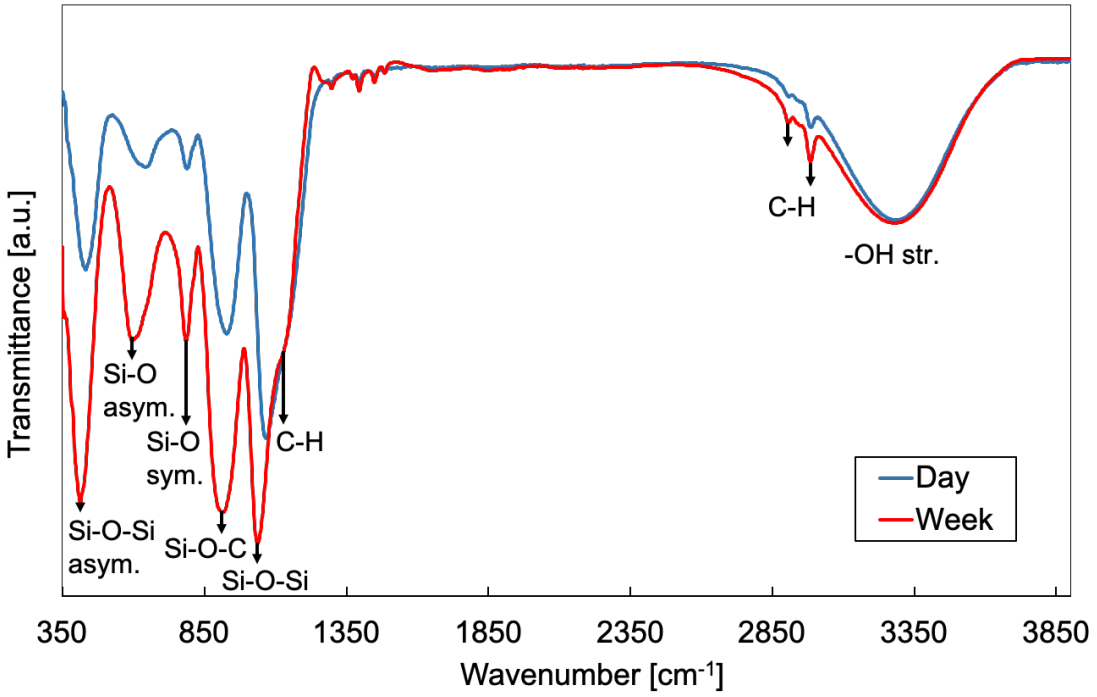


**Figure 4.3:** FTIR (ATR) transmittance spectra of the sol 1 hour, and 1 week after synthesis with a proposed assignment of structural groups. The time dependent difference in peak intensities indicate that the hydrolysis and condensation reactions were not terminated after 2 hours of synthesis.

## 4.3 Slurry Characterization

This chapter provides information on physical appearance and structural composition in GO and CuO slurries. The GO concentrations were chosen based on results from previous work conducted by the author [10], where it was found that slurry stability improved by increasing the GO concentration. This was examined by visual observation and by measuring the zeta potential. The images and zeta potential measurements from the specialization project are included in Appendix C.

### 4.3.1 Slurry appearance

The slurry appearances are imaged in Figure 4.1 for GO and 4.2 for CuO. All GO slurries have relatively high concentrations of GO to avoid uncertainty regarding phase separation. In GO C-100, phase separation in the top layer is visible. The upper phase is assumed to be EtOH. GO C-125 and C-150 can only be separated by color and the slurries are found to be more stable. For GO, there were no difference in slurry appearance over time.

The CuO slurries were observed to be very unstable, and particles quickly precipitated in the suspension. As a consequence, the slurries were sonicated before deposition to substrate. Visual appearance before and after sonification are provided in Figure 4.2. All CuO slurries appeared the same, without any significant differences, and only CuO C-125 is used to illustrate appearance.

Zeta potentials may have described the stability characteristics and reveled differences in electrical potentials in the interfacial double layer in all the dispersions, but was not possible to measure due to high particle concentration and dark color.

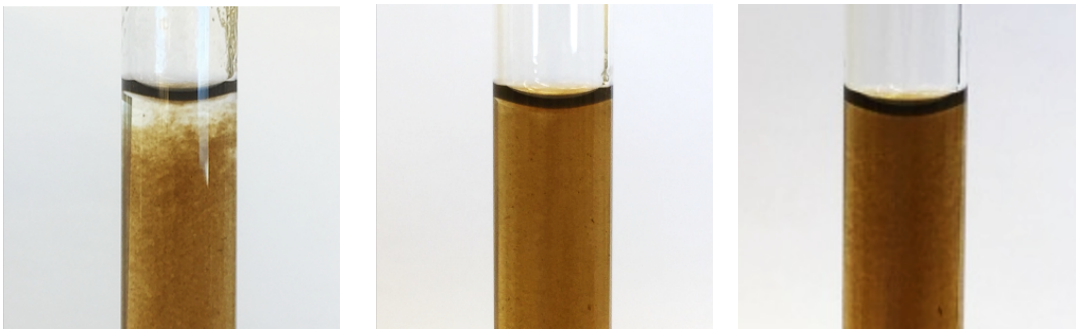

**(a)** C-100 **(b)** C-125 **(c)** C-150

**Figure 4.1:** Visual appearance of the GO slurries a) C-100, b) C-125 and c) C-125. C-125 and C-150 are observed to be the most stable dispersions. The slurries characteristics did not to change over time.

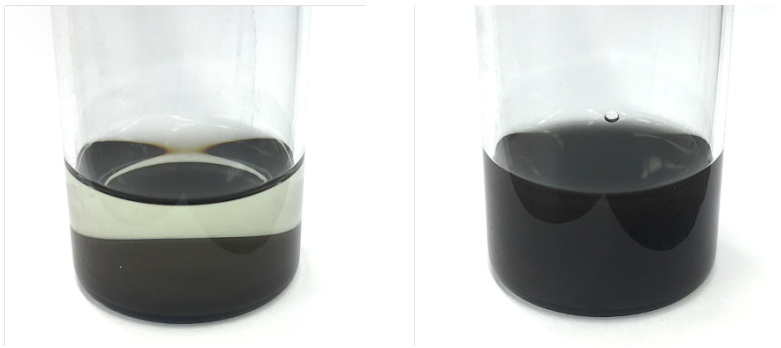

**(a)** C-125 before sonification **(b)** C-125 after sonification

**Figure 4.2:** Visual appearance of CuO C-125 a) before and b) after sonification and preparation for coating deposition. The slurry is not stable and phases separates quickly.

### 4.3.2 Raman spectroscopy

Raman spectroscopy was used to reveal potential changes in GO carbon structure after mixing GO and sol. The D and G peaks from raw data, for all GO slurries are plotted in Figure 4.3. Results for pure GO paste is added for comparison. The G peak is found at Raman shift 1340 $cm^{-1}$ and the G peak at 1590 $cm^{-1}$. The peaks were deconvoluted and peak intensities and ratios for each slurry are given in Table 4.1. The slurries were dried before analysis and can be described as xerogels.

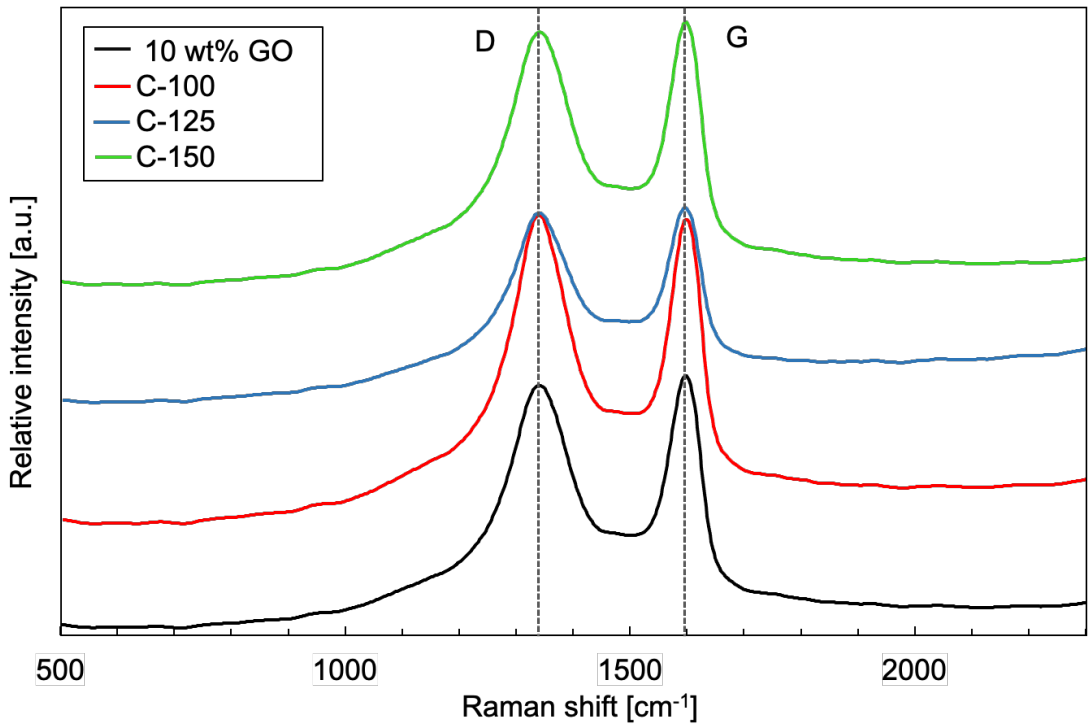


**Figure 4.3:** Comparison of Raman spectra for GO containing coating slurries before deconvolution and curve fitting. The D band position is ∼1340 cm−1 and the G band is positioned at ∼1590 cm−1.

**Table 4.1:** Peak values for D and G bands from Figure 4.4

| Coating ID | D Band | G Band | $I_D/I_G$ |
|---|---|---|---|
| 10wt% GO | 7253 | 6424 | 1.13 |
| C-100 | 7893 | 6012 | 1.31 |
| C-125 | 4690 | 3746 | 1.25 |
| C-150 | 6980 | 5864 | 1.19 |

From Table 4.1, it is proven that the intensity ratios decrease for increasing GO concentrations, from 1.31 for C-100 to 1.19 for C-150. This imply a reduction in defects in the carbon structure when GO concentration is high. The pure GO material provide an intensity ratio of 1.13.

## 4.4 Coating Characterization

### 4.4.1 SEM imaging and EDS analysis

**Graphene Oxide**

In the specialization project, the substrates were coated in six layers, making the final coating thick and provoked crack formation [10]. Hence, an optimization of coating thickness was needed. Images from previous work is included in Appendix D. All slurries were coated 1-5 layers on steel substrates, where 3 layers were observed to be the most promising, for a desired even surface. In Figure 4.1 the coating surfaces are imaged. C-ref was observed to undergo crack formation at a high number of layers and C-100 were not homogeneous for lower number of coating layers. Figure 4.2 captures the two cases. A clear change in surface structure can be attended after GO were added. The arrows in image Figure 4.1 b) show areas in C-100 revealing uncoated steel substrate. There were no difference in appearance between C-125 and C-150.

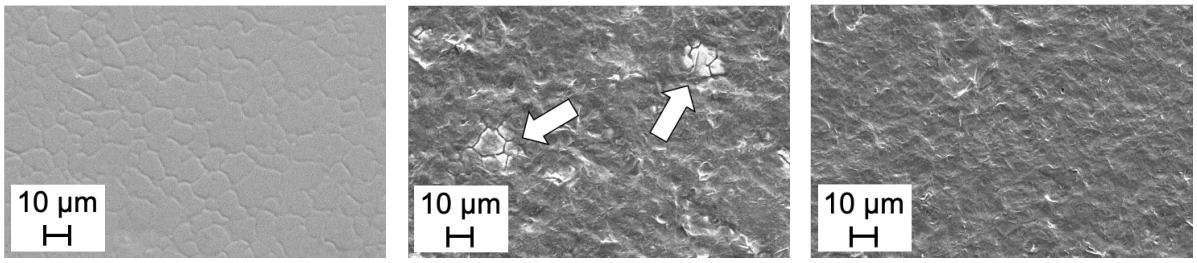


**(a)** C-ref **(b)** C-100 **(c)** C-125

**Figure 4.1:** SEM images of the GO coatings a) C-ref, b) C-100 and c) C-125. There were no difference in appearance between C-125 and C-150.

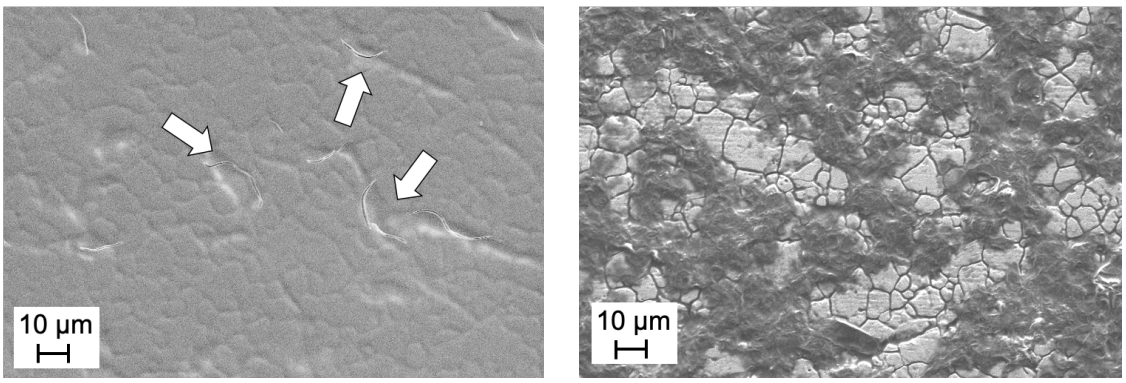


**(a)** Five Layers C-ref **(b)** One Layer C-100

**Figure 4.2:** SEM images of coating a) C-ref 5 layers and b) GO C-100 1 layer. Arrows are pointing at coating cracks in a). Larger areas of uncoated steel are visible in image b).

EDS point analysis was performed on 1 layered GO C-100. From the analysis it was confirmed that the uncoated area was revealed steel sample, with iron and chromium being the abundant elements. Traces of silicon and oxygen was also found. Si and O were the abundant elements on the coated surface. High uncertainty is related to detection of light elements, and analysis of carbon compounds and presence of GO in coating surface is not possible to determine. The visible change in surface structure supports the assumption of GO being on or close to coating surface.

**Copper Oxide**

The SEM image in Figure 4.3 illustrates how CuO agglomerates on the surface after coating preparation. Point detection EDS analysis confirms the agglomerated areas (B) are CuO particles as Cu and O are two of the abundant species. The final coatings were observed to endure crack formation this is observed in the left image in Figure 4.3. By increasing amount of CuO additive, the only observed difference in coating appearance is the increasing size of agglomerates.

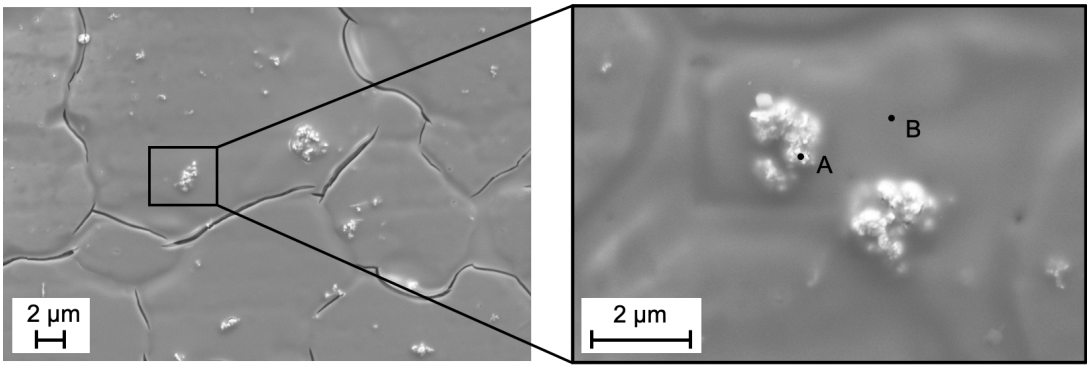


**Figure 4.3:** SEM images of CuO C-125. The points marked A and B in the right image are positions for EDS point analysis. Point A provide high intensity for Cu, Si and O, while in point B, Si and O are the abundant species.

### 4.4.2 Coating thickness

Charging effects due to non conductive materials in epoxy-cast samples, caused issues for reliable results for determination of coating thickness and element analysis (EDS). The polished samples were sputtered with gold to eliminate charging. Figure 4.4 provides the SEM images of what is presumed to be the coating layer in GO C-125. The thickness is found to vary from ∼40-50 $\mu$m. The procedure for polishing did not provide a flatten cross section. Similar structures to Figure 4.4 were observed in the other samples, but not as a continuous phase, and identification of coating layers was uncertain. Cross sectional EDS mapping analysis were not manageable after coating with gold, and the conducted results are not reliable.

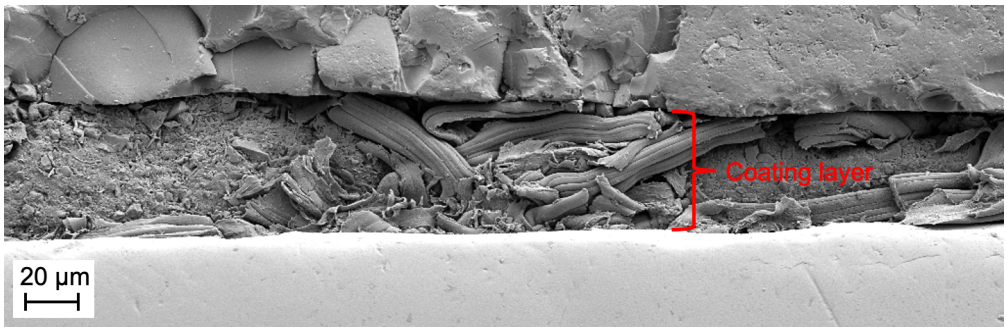


**Figure 4.4:** SEM images of GO C-125 cross section. Coating thickness is found to measure ∼40-50 $\mu$m.

### 4.4.3 AFM imaging

AFM images displaying the topography of the silica and GO coatings are provided in Figure 4.5. Areas of 100 $\mu m^2$ (10$\mu$m ·10$\mu$m) were scanned by tapping mode. The raw data was edited upon line removal and a third degree polynomial fit by the software Pico Image Basic. The maximum sample heights (Z-axis values) are listed in Table 4.1. Additionally, color maps and sample profiles are given in Figure 4.6. The dashed lines provided in the the color maps represent the plotted profiles (from red to green marker). Maximum peak to valley height of the profiles, $P_t$, and the calculated average arithmetic surface roughness, $R_a$, are listed in Table 4.1. C-125 exhibit the highest surface roughness of the samples analysed with $R_a$ value 0.14 $\mu$m. In general, the roughness increases with increasing amount of GO additive.

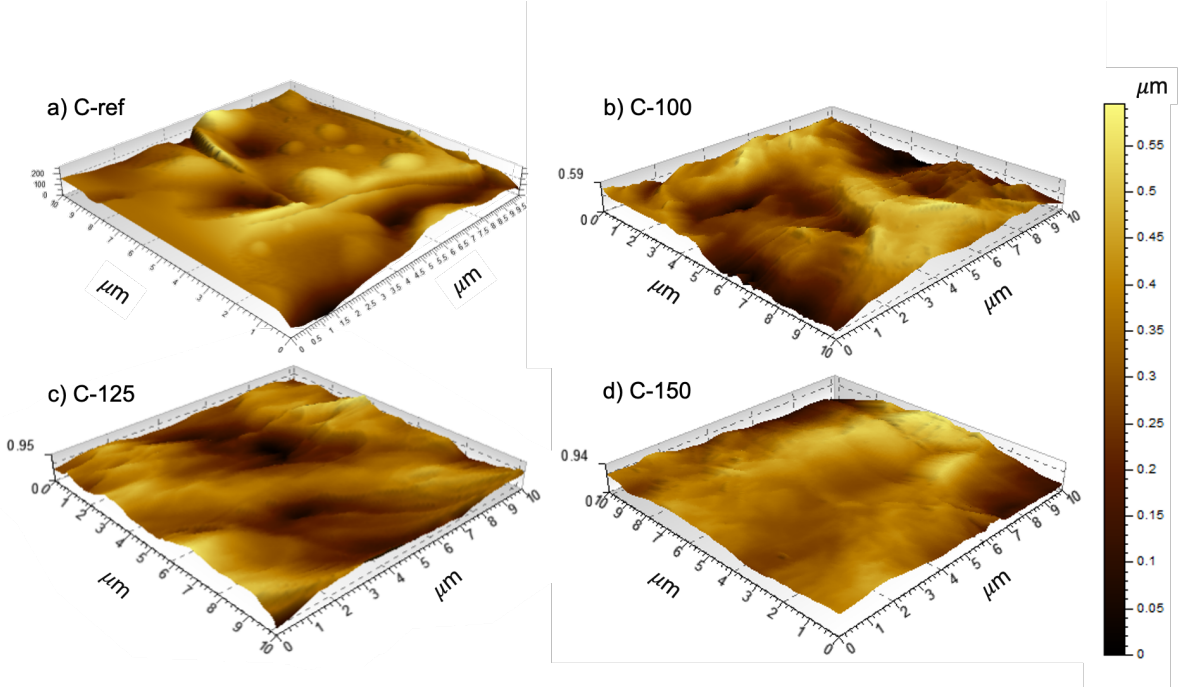


**Figure 4.5:** AFM topography images of the GO coatings a) C-ref, b) C-100, c) C-125 and d) C-150. Pico Image Basic was used for topography 3D imaging and data analysis.

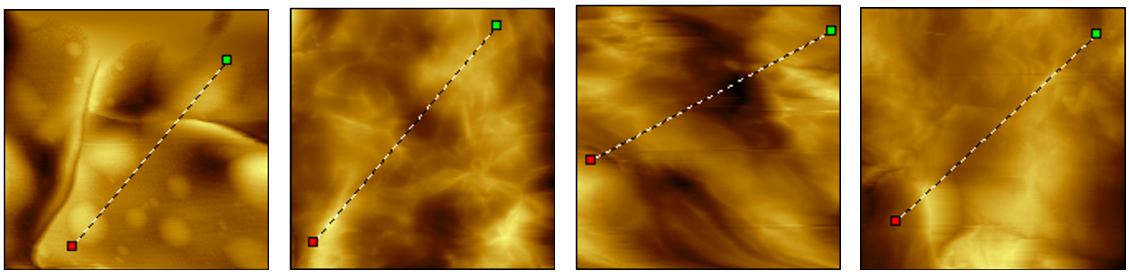

**(a)** C-ref **(b)** GO C-100 **(c)** GO C-125 **(d)** GO C-150

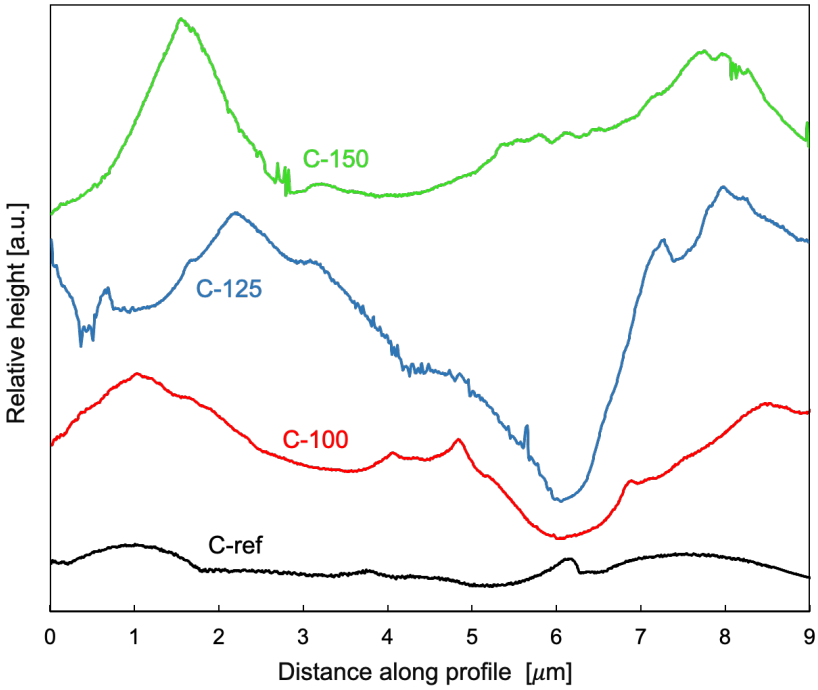


**Figure 4.6:** AFM color-map images and plotted profiles of a) C-ref, b) C-100, c) C-125 and d) C-150. The plotted profiles correspond to the dashed lines in color map captions (from red to green marker). The images and profile data were obtained from Pico Image Basic software for AFM data analysis.

**Table 4.1:** Sample height and average arithmetic surface roughness, $R_a$ for silica and GO coatings from AFM analysis.

| Coating ID | Z-axis [$\mu$m] | $P_t$ [$\mu$m] | $R_a$ [$\mu$m] |
|---|---|---|---|
| C-ref | 0.27 | 0.097 | 0.021 |
| C-100 | 0.55 | 0.36 | 0.068 |
| C-125 | 0.96 | 0.68 | 0.14 |
| C-150 | 0.95 | 0.42 | 0.083 |

### 4.4.4 Contact angle measurements

The reported contact angles for silica and GO coatings are given as the average of three measurements executed at different positions on the coated steel samples. The edges were avoided due to possible edge effects and deviations from characterized structure. The contact angles for CuO origin from only one measurement. The reason being difficulties in recording data for low contact angles approaching complete wetting. The measured contact angles for three layer coated samples are provided in Figure 4.7.

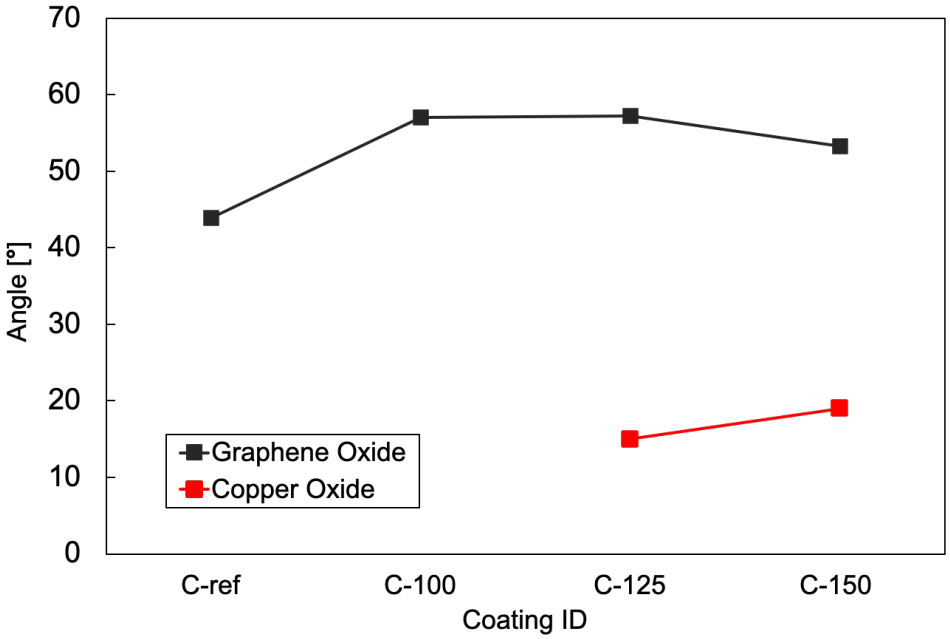


**Figure 4.7:** Contact angle measurements for three layer GO and CuO coatings compared to reference silica coating.

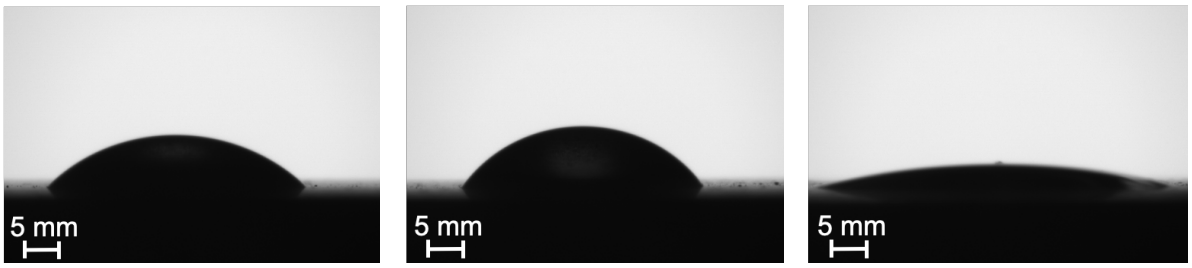


**(a)** C-ref **(b)** GO C-100 **(c)** CuO C-100

**Figure 4.8:** Captions of one of the measured contact angles for a) C-ref, b) GO C-100 and c) CuO C-100 0.5 s after water droplet deposition. CA for C-ref is here 44.6° ±0.4 and 56.7° ±0.3 for GO C-100. The CA for CuO C-100 was not measurable due to high wettability.

All measured contact angles lie within the hydrophilic region (< 90°). CuO coatings exhibit high degree of wetting ∼20°for C-125 and C-150. For C-100 the contact angle was

too low for measurement. The GO coatings behave less hydrophilic with contact angles at ∼55°. The reference silica coating has contact angle ∼45°. Figure 4.8 illustrates the visual difference in contact angles between C-ref, C-125 GO and C-150 CuO. The droplets are imaged 0.5 seconds after deposition. Contact angle measurements for all silica and GO coatings (1-5 layers) were conducted and are provided in Appendix E.

### 4.4.5 Micro scratch tests

Plotted scratch profiles of three layer C-ref and GO C-150 coated on steel, are provided in Figure 4.9 a)-b). The plots include penetration depth and residual depth, and are compared to a clean steel sample in Figure 4.9 c).

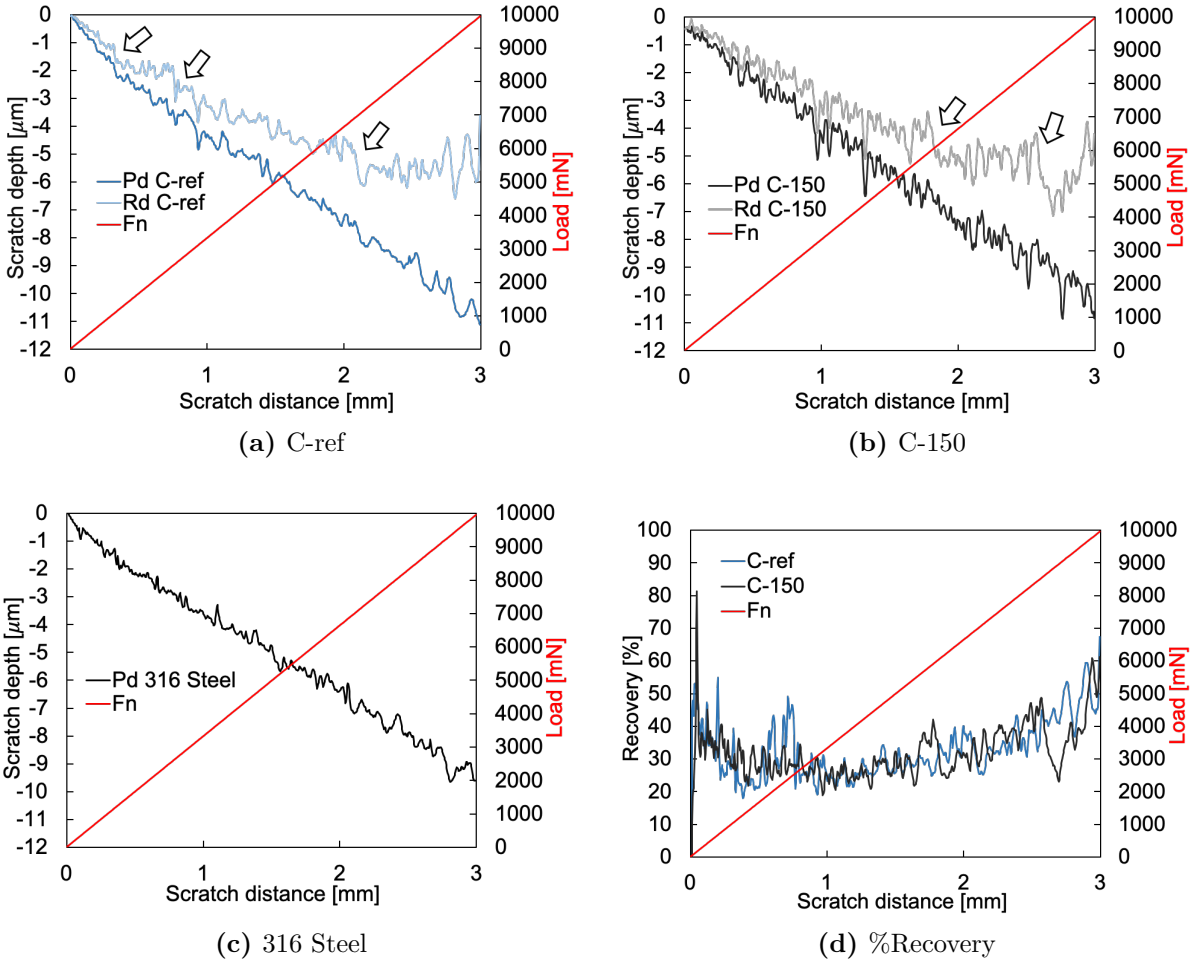


**(a)** C-ref **(b)** C-150

**(c)** 316 Steel **(d)** %Recovery

**Figure 4.9:** Scratch penetration depth ($P_d$) at progressive load (30-10,000 mN) and residual depth ($R_d$) at constant load (30 mN) for a) C-ref and b) C-150 over a distance of 3 mm. C-ref starts to break at ∼1200 mN and C-150 at ∼6000. c) is $P_d$ for uncoated 316 steel substrate. The coating recovery, d)%Recovery, varies the most for C-ref at lower loads and at higher loads for C-150.

The adhesion strengths are determined by observing a drop in scratch depth in the residual profiles, pointed out by arrows. C-ref suffer from rupture from initial loads, but at ∼2650 mN a significant drop in penetration depth is observed. C-150 starts to wear off the steel from 6130 mN. This is confirmed by the OM images in Figure 4.10. Recovery percentage along the scratch lengths are provided in Figure 4.9 d). % recovery fluctuates for C-ref at initial loads and for C-150 at higher loads (from ∼6000 mN). In general, recovery is higher for higher loads ( ∼50%). A complete comparison of initial rupture for all GO coatings is made in Table 4.2. The belonging scratch profiles and %recovery are provided in Appendix F.

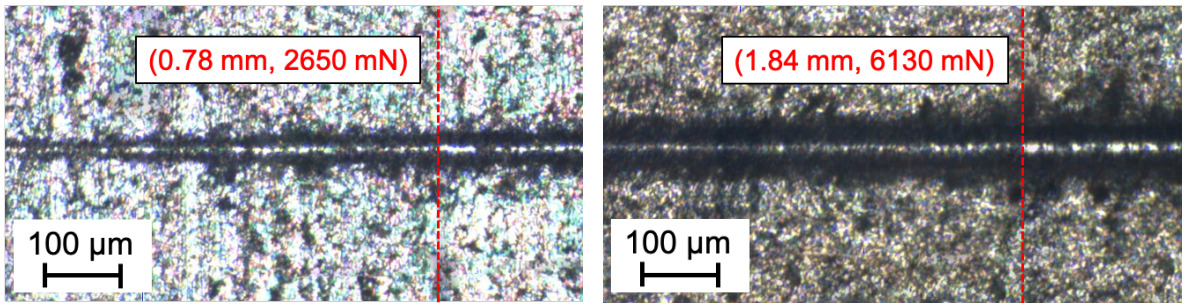


**(a)** C-ref **(b)** C-150

**Figure 4.10:** Optical microscope images of scratches in a) C-ref and b) C-150. The images correspond to plotted scratch profiles in Figure **??** a) and b).

**Table 4.2:** Approximately load at initial rupture [mN] for the considered coatings based on scratch profiles and observations in optical light microscope.

| Coating ID | Initial rupture [mN] |
|---|---|
| C-ref | 1870 |
| C-100 | 4082 |
| C-125 | 6206 |
| C-150 | 6129 |

## 4.5 Biofilm Characterization

All surfaces were examined in SEM after termination of the bacteria growth experiments. This section provides images from all the experimental work in the biofilm reactor. Number of bacteria in the SEM images were counted and are converted to Table 4.1. Due to low distribution of anti-fouling material and poor wear resistance for the experimental parameters, the CuO coating results on bacteria growth are limited. The number of bacteria found on these samples are not comparable to the GO coating results are not presented in the table.

### 4.5.1 Short term experiments

Four different experiments were conducted for 1 week, varying the anti-fouling agent and access to nutrients. SEM images illustrating a representative view on bacteria growth on the sample surfaces are provided in Figures 4.1-4.4.

**Graphene Oxide Coatings without f/2**

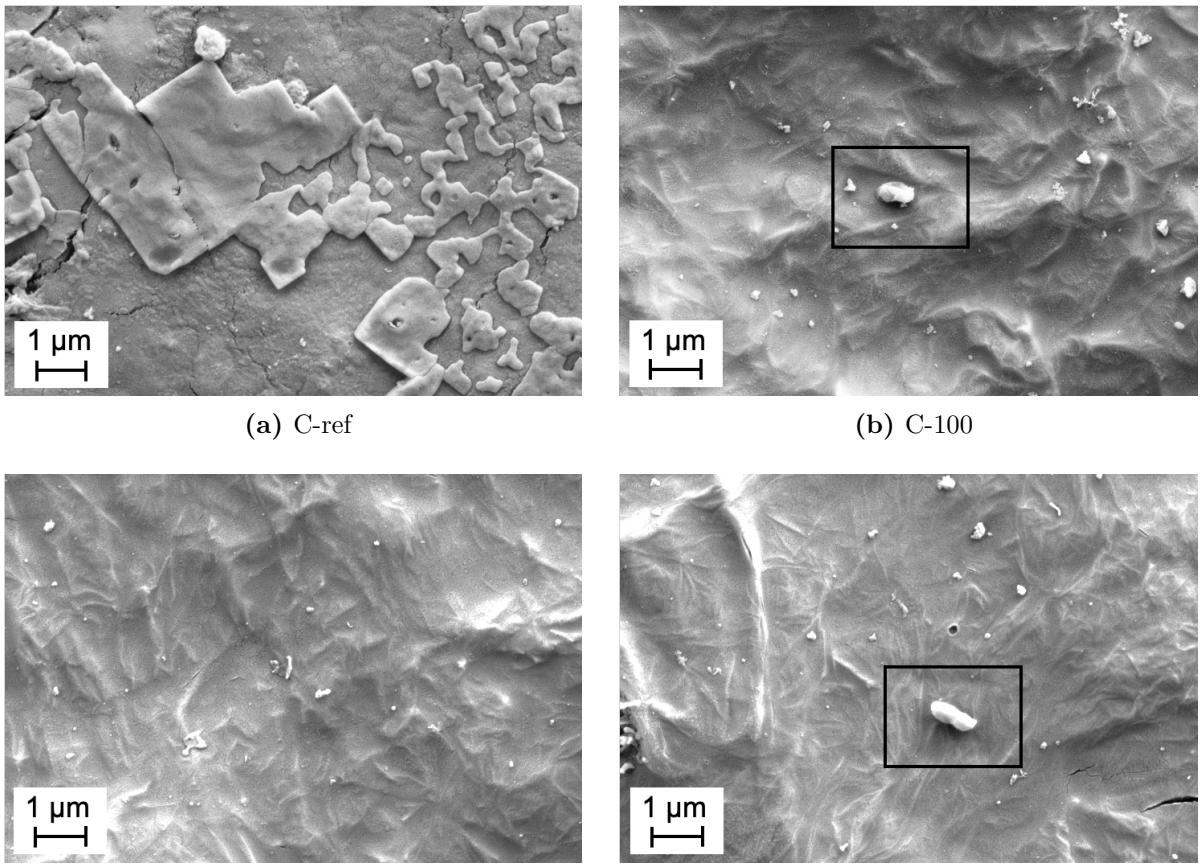


**(a)** C-ref **(b)** C-100

**(c)** C-125 **(d)** C-150

**Figure 4.1:** Comparison of bacteria growth on GO coated surfaces between week 1 and 2. Black frames highlight bacteria on surfaces with limited growth.

### Graphene Oxide Coatings with f/2

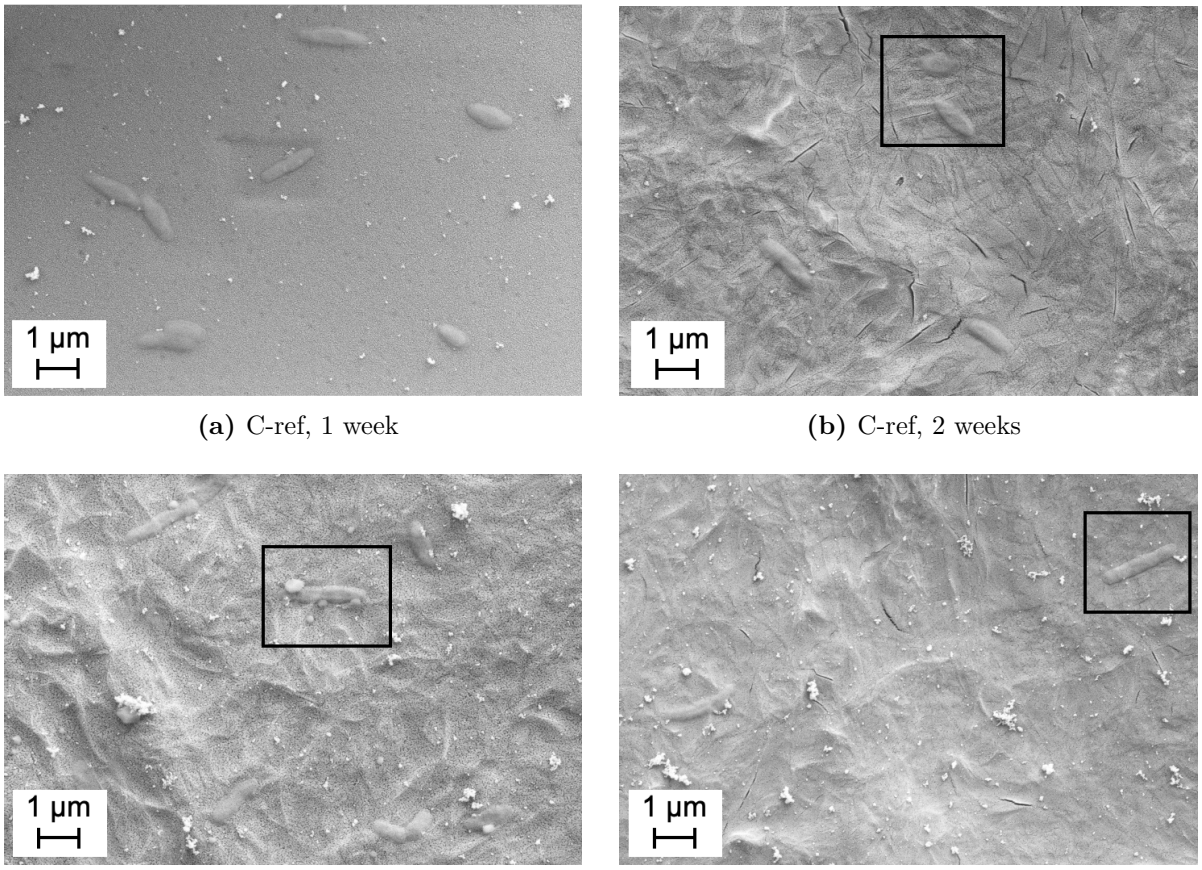


**(a)** C-ref, 1 week

**(b)** C-ref, 2 weeks

**(c)** C-100, 1 week

**(d)** C-100, 2 weeks

**Figure 4.2:** Comparison of bacteria growth on GO coated surfaces between week 1 and 2. Black frames highlight bacteria on surfaces with limited growth.

In the one week experiments, the effects of f/2 is observed in particular. f/2 improves the growth conditions, and an increase from one observed bacteria in Figure 4.1, to up to ten bacteria observed for a comparable sample in Figure 4.2, confirms this. In both experiments with GO, there were not observed any difference regarding growth between the reference and the coated samples.

In the copper oxide coating, the additive agglomerated on the surface, leaving large areas of silica coating without incorporated additive, hence the effect of additive could not be determined. There were also found cracks in the coating as illustrated in Figure 4.3 a). There are little foulants present in the experiment without f/2 in Figure 4.3, similar to the results for GO. When f/2 was added to the water, the increase in particles seem to wear off the coating, only leaving small spheres of coating left on the surface, as observed in Figure 4.4b). A cluster of bacteria is observed on the substrate surface in 4.4a).

**Copper Oxide Coatings without f/2**

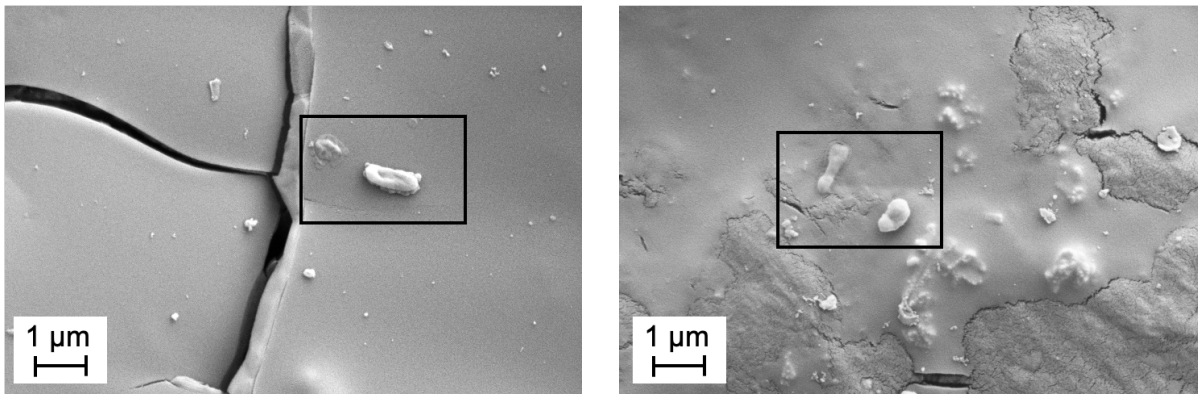


**(a)** C-ref, 1 week **(b)** C-ref, 2 weeks

**Figure 4.3:** Surface appearance after 4 weeks submerged in seawater. Crystallization of salts causes high uncertainty to the observations of bacteria.

**Copper Oxide Coatings with f/2**

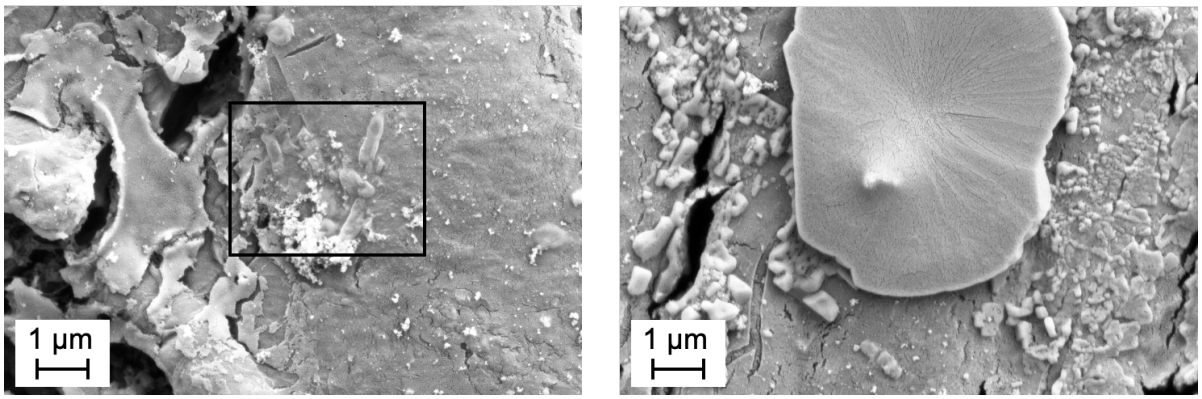


**(a)** C-ref, 1 week **(b)** C-ref, 2 weeks

**Figure 4.4:** Surface appearance after 4 weeks submerged in seawater. Crystallization of salts causes high uncertainty to the observations of bacteria.

### 4.5.2 Long term experiment

One experiment was run for four weeks with GO as anti-fouling material. SEM images from the experiment are given in Figure 4.5. Results from the long term experiments show that the reference silica coating exhibit low wear resistance, and the observed bacteria growth for C-ref is occurring on the substrate surface. From the GO coated surfaces, there are observed clear differences in growth extension between week one and week two, and considerable numbers of bacteria are released from the surface. Distribution of bacteria is observed to be low for C-150.

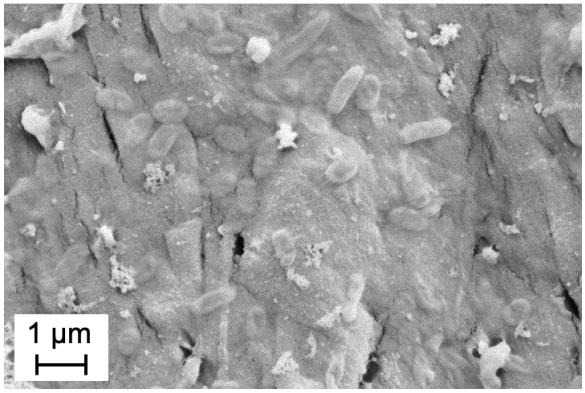


**(a)** C-ref, 1 week

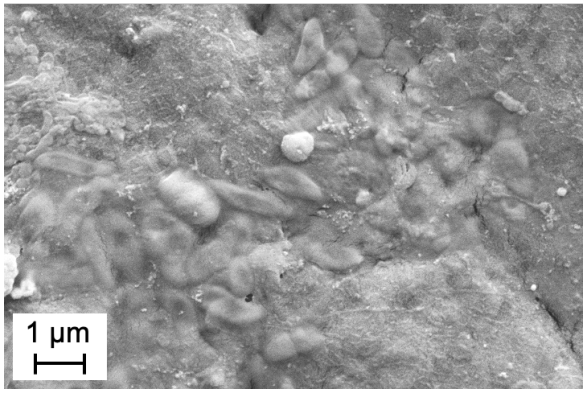


**(b)** C-ref, 2 weeks

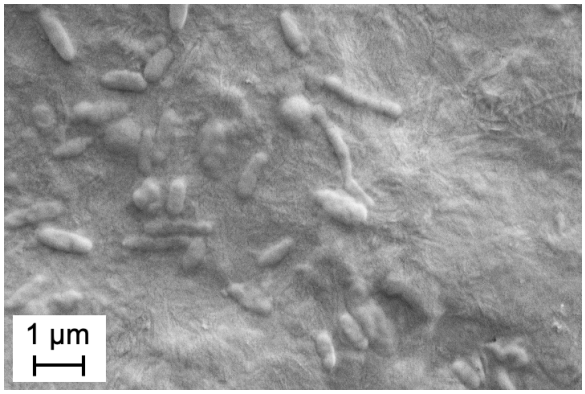


**(c)** C-100, 1 week

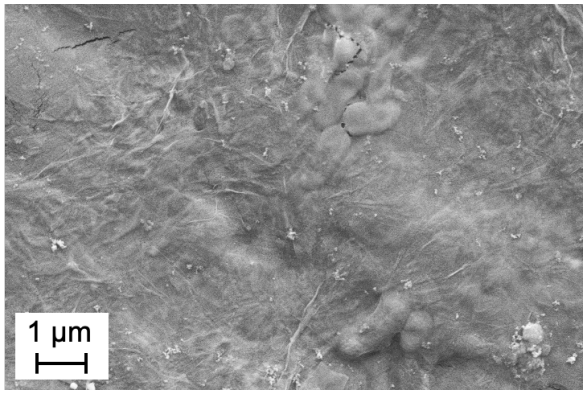


**(d)** C-100, 2 weeks

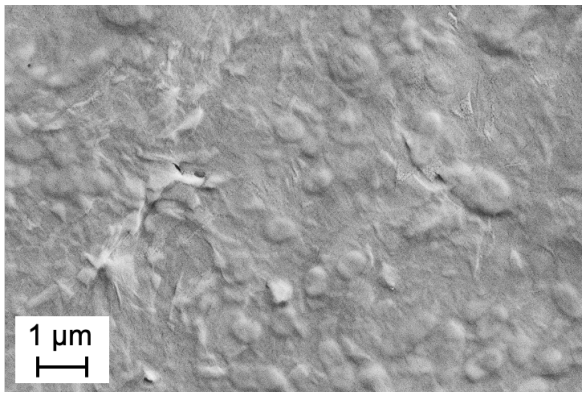


**(e)** C-125, 1 week

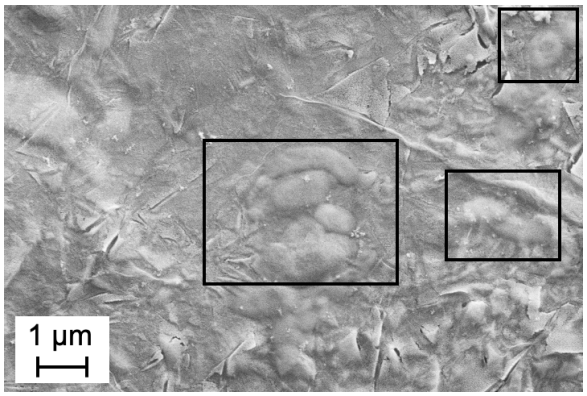


**(f)** C-125, 2 weeks

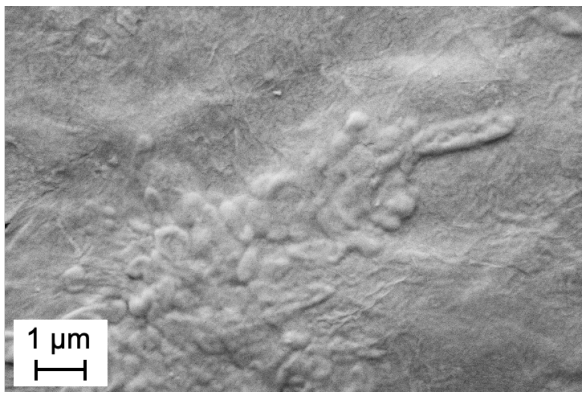


**(g)** C-150, 1 week

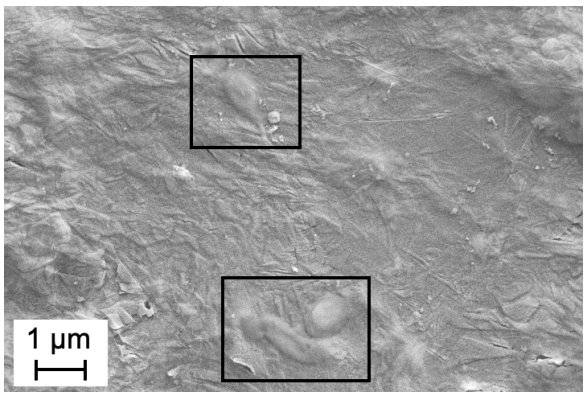


**(h)** C-150, 2 weeks

**Figure 4.5:** Comparison of bacteria growth on GO coated surfaces between week 1 and 2. Black frames highlight bacteria on surfaces with limited growth.

Figure 4.6 provides sample images after four weeks in the biofilm reactor. Crystallization of salts interrupt the biofilm characterization, and bacteria are difficult to identify. Results regarding bacteria growth were not reliable after a period of four weeks.

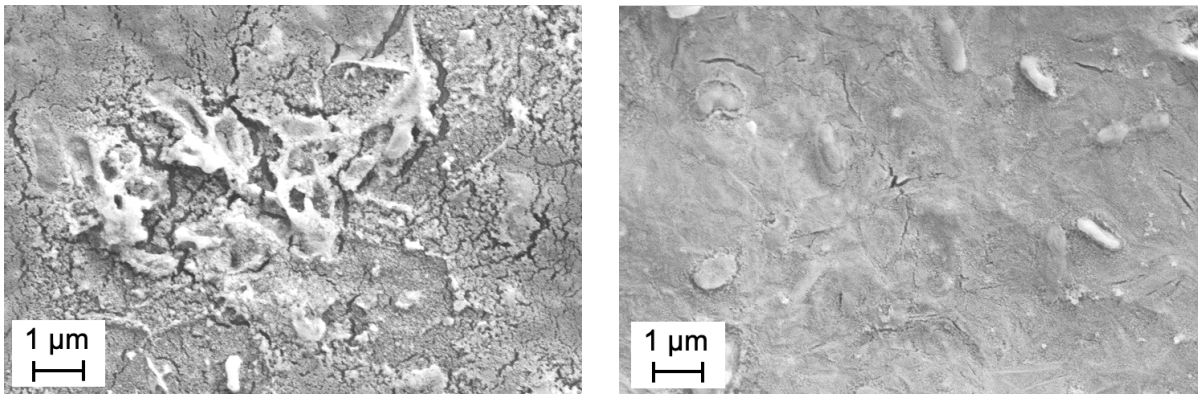


**(a)** C-ref, 1 week **(b)** C-ref, 2 weeks

**Figure 4.6:** Surface appearance after 4 weeks in the biofilm reactor. Crystallization of salts causes high uncertainty to the observations of bacteria.

### 4.5.3 General observations

From previous images and Table 4.1, there is observed to be no visual difference in growth between the coatings after one week, but f/2 does improve the growth conditions. For longer periods than one week, reductions in bacteria growth is visible and effects of anti-fouling properties can be assumed.

**Table 4.1:** Number of bacteria (NoB) on reference and GO coated substrates after biofilm experiments (three experiments divided in sections). The values are adapted from SEM images provided in present chapter.

| Coating ID | f/2 | 1 week [NoB] | 2 weeks [NoB] | 4 weeks [NoB] |
|---|---|---|---|---|
| C-ref | no | N/A | - | - |
| C-100 | no | 1 | - | - |
| C-125 | no | 0 | - | - |
| C-150 | no | 1 | - | - |
| C-ref | yes | $< 10$ | - | - |
| C-100 | yes | $< 5$ | - | - |
| C-125 | yes | $< 10$ | - | - |
| C-150 | yes | $< 5$ | - | - |
| C-ref | yes | $> 30$ | $> 30$ | N/A |
| C-100 | yes | $> 30$ | $< 15$ | N/A |
| C-125 | yes | $> 30$ | $< 15$ | N/A |
| C-150 | yes | $> 30$ | $< 5$ | $< 10$ |

# 5 Discussion

The aim of the work was to look at the anti-fouling performance to graphene oxide in coatings, and compare these result to the effects of copper oxide, a well-studied material for anti-fouling purposes [11]. The silica coating does not exhibit the mechanical properties or performance required for use in any marine industry. Hence, the coatings are limited to scientific studies and are not suited for final industrial objectives. The sol-gel process is a simple and cost-effective production route, and suitable for the aim of studying the concept of growth inhibiting properties, in the GO material provided. The first part of this section concerns the results from the growth experiments and possible associated mechanisms. Material characterization is conferred in the next section, followed by reviews on coating synthesis. In the final section, coated surface characteristics are discussed and includes possible effects on bacterial growth.

## 5.1 Assessment of Bacteria Films

### 5.1.1 Short term experiments

The biomass production is low in the short term experiments due to low initial concentration of bacteria. f/2 increases the biomass production, and the marine enrichment is found to be an efficient way to make the environment more challenging regarding biofilm production. This makes it easier to examine the anti-fouling effects in shorter terms. A proposed solution for experimental improvements regarding reproducibility, is to control the amount and type of bacteria added, and make a bacteria stock solution.

From the experiments without f/2, the growth is too low to make a conclusion on the effect of the GO additive. Bacteria seem to attach to sample surface in a random manner. From this result, and the fact that the coating is applied parallel to the substrate surface, it is assumed that cell disruption due to sharp edges in GO, is not the main mechanism for antibacterial activity, as bacteria seem to adhere to any surface.

In the copper oxide coating the CuO agglomerated, and left large areas of silica coating without any incorporated additive. The issues related to agglomeration makes it difficult to conclude on the effects of CuO as anti-fouling agent in the prepared coating. When

f/2 was added to the experiment, the increase in particles seemed to cause increased wear and rupture, only leaving small spheres of coating left on the surface. The coating is very hydrophilic and CuO dissolves well in water. As a consequence, CuO were released uncontrolled into the seawater and might have extinguished the bacteria stock, due to high toxicity. There were observed very limited growth on all samples in the experiment, despite the addition of f/2. The copper oxide coatings did also suffer from crack formation. A possible explanation is increase in cohesive forces between dispersed particles and agglomerated during drying, since the cracks were observed to surround the agglomerates.

### 5.1.2 Long term experiments

The reference silica coating were found to exhibit low wear resistance, and the observed bacteria growth for C-ref is occurring on the sample surface. From the GO containing coatings, there were clear differences in growth extension between week one and two, and the reduced number of bacteria proved that GO exhibit antibacterial properties. Figure 4.5 show that most of the bacteria are released from the surface. Hence, the trapping mechanism (bacteria are folded in graphene sheets), proposed in Section 2.5 were assumed to be a limited contribution to growth inhibition. Oxidative stress and production of reactive oxygen species, is the proposed mechanism presumably causing the anti-fouling effects, and agrees well with the work conducted by Liu et al [8]. Since the oxygen groups will be a limited resource by contribution to ROS, the anti-fouling effects is presumably time dependent, and coating maintenance will be necessary after a certain period of time.

There are several parameters causing uncertainties in the obtained results. The variation on bacteria concentration is mentioned, but bacteria composition may have an affect, as GO seem to have various growth inhibiting effects on different types of bacteria [8]. Water evaporation leading to saturation and salt crystallization on the samples, is also a problem for determination of number of bacteria. This was observed in several growth experiments. To avoid evaporation, the biofilm reactor should be a closed system or be diluted. A closed system will remove the oxygen access and prevent growth. A possibility is to do the same experiment in freshwater. The low light access, due to the cover of water bath balls, might also cause error in the final results, as light is a key resource for bacteria growth [15]. Regarding the assessment and quantification of biofoulants, no standardized quantitative tests were preformed and the reproducibility is low.

## 5.2 Graphene Oxide Material Characteristics

The GO material provided, contained 62.4 at% Carbon, 37.5 at% Oxygen, found in Table B.1. Hence, the functionalization of oxygen containing groups was assumed to be significant. In the Raman spectrum, the observed peak intensity ratio were 1.13, and this indicate a relatively low fictionalization of oxygen groups. For comparison, in a similar study by Pieper et al. [68] $I_D/I_G$ was 3.0 for the GO material. Reasons for the high level of graphite structured carbon, is not known due to limited information on production procedure.

To enhance the understanding of the graphene oxide properties, further characterizations were necessary. SEM and XRD analysis, proved the presence of GO in the material provided, this by observing the material morphology, and the characteristic diffraction peak at $2\theta = 11.9°$corresponding to lattice plane (001). FTIR spectum confirmed presence of hydroxyl, carboxyl, epoxide and carbonyl groups in the GO material. The frequency band at $\sim$1600 $cm^{-1}$ in the FTIR specra is assumed to be C=C bonds.

## 5.3 Coating Synthesis

In the following section, sol characteristics will be discussed with respect to the chosen sol parameters. The slurry preparation and coating deposition are also of concern.

### 5.3.1 Sol characteristics

The chosen synthesis route was found to work well for the objectives in this work. The acid catalysed sol provided a dense coating with hydrophilic properties. The hydrophilicity of the silica coating is temperature dependent [44] and higher wattability could have been obtained by higher temperatures in the heat treatment step. The chosen temperature of 60° was based on the maximum operational temperature to PE ($\sim$65°C).

In the obtained FTIR specta of the sol, Figure 4.3, there were observed C-H bonds, which indicates the presence of $-OC_2H_5$ groups in the final structure. These are hydrophobic groups that reduce the hydrophilic character in the coating. Based on work by Ye et al. [44], the $-OC_2H_5$ groups are removed by increasing the heat treatment temperature (400°C).

The viscosity was found to be constant over time and the sol did not change character. The low viscosity values are explained by the high molar ratio of solvent in the synthesis. The rheological properties made it possible to utilize the sol for longer periods of time after synthesis. The only concern was the reaction time. The hydrolysis and condensation reactions were not terminated after 2 h of synthesis. This was observed in the FTIR spectrum (Figure 4.3), and the increase in detected silicon and oxygen bonds from one

day to one week. The coating additives were not mixed with the sol until one week after synthesis.

### 5.3.2 Graphene oxide stock solution

Since EtOH was the solvent used in the sol-gel process, it was decided to disperse GO in EtOH to avoid unwanted interactions with water. The GO stock solution was sonicated for 2 minutes. This is found to be the best compromise for graphene materials regarding mixing, and possible breakage of bonds and loss in mechanical properties [69].

### 5.3.3 Slurry stability

Both the GO C-100 and all CuO slurries were unstable suspensions and separated quickly. CuO could have been added in lower concentration to reduce particle collisions and the attractive forces between agglomerates. This might have obtained a more stable dispersion.

The phase separation in C-100 is explained by the low concentration of GO, as stability is found to increase for increasing consecrations. A theory is that the edge groups of the siloxane particles in the sol, reacts with the oxide groups on the graphene oxide sheets in a condensation reaction. Then, GO sheets will point out from the particles. The particles become more bulky the more GO that is present and is able to react. Large particles stabilizes the dispersion by steric hindrance.

### 5.3.4 Assessment of Raman spectra

The Raman spectra show there are less defects in the graphene structure in C-150, compared to C-100 and C-125, shown i Table 4.1. This may be caused by residual GO, not reacting with the siloxane groups in the sol, and the peak intensity ratio is therefore closer to pure GO. Both steric and electrostatic hindrance are believed to stabilize the slurries. This has been established in previous work and can be observed in Figure C.1 [10].

Raman spectra was extracted from dried suspensions (xerogels) and not from the final coatings. Defects in carbon increases with increasing temperature, but since the heat treatment stage between xerogel and coating state was preformed at a relatively low temperature, 60°C (333 K), it is believed to not change the amount of defects dramatically. It is assumed that only evaporation of solvent occurs in the heat treatment step in the synthesis. For comparison, pyrolytic carbon formed at 1000 K, provides a similar structure to graphite, but is high in structural imperfections, by binding graphene sheets together in covalent bonds [70].

By observing the Raman peak intensities in Figure 4.1, they are considerably lower for C-125 compared to the other examined samples. A possible reason is poor resolution in the examined positions on the sample surface. However, the peak intensity ratio is constant, and the result of 1.25 $I_D/I_G$ seems reasonable as it lies within the range of results for C-100 and C-150 (1.19 and 1.31 respectively).

### 5.3.5 Coating deposition

Spray coating was chosen as deposition method because it is directly related to the coating techniques used for vessels and offshore structures. The slurries were shaken before they were sprayed to the substrates to make the final coating as homogeneous as possible. The CuO slurry was sonicated to ensure mixing of particles. A thickness of three layers, was the optimal number of coating layers to achieve a homogeneous surface structure without cracks. The result only include GO coatings. Three coating layers were found to correspond to a thickness of $\sim 40 - 50\mu$m, but this result is of high uncertainty. Cracks and any reveal of substrate surface have the potential of an increased bacteria growth and was.

## 5.4 Surface Characteristics and Coating Performance

### 5.4.1 Coating adhesion strength

There are found no distinct reason for C-125 to exhibit a higher rupture load compared to C-150, as observed in Table 3.2. However, the general trend show that coatings with high GO concentrations and homogeneous surface structure, are more wear resistant compared to reference sample and C-100.

Wear from current and particles in the seawater may cause rupture and reveal substrate surface. From the SEM images in section 4.5, non of the GO coatings seem to suffer from rupture, and are not found to effect the number of bacteria between the GO coated surfaces. The adhesive strengths to PE were not investigated in this thesis, but it will be relevant for further work. Especially in specialization toward a certain field of application and construction material.

### 5.4.2 Contact angle measurements and surface roughness

With respect to anti-fouling properties, growth inhibition might be explained by both chemical and structural characteristics. Hydrophilic surfaces are in general more suitable for anti-fouling use, but this were not properly tested in this thesis. All coated surfaces were found in the hydrophilic range. The low contact angles for CuO coating were expected due to the hydrophilic properties of CuO in contact with water. Wenzel's

Equation 2.2 implies that the contact angle for GO surfaces could be of a more hydrophobic character if the roughness was lower. The hydrophobic character can be explained by the abundance of graphite structure in the GO material. The relatively high contact angels for the reference silica sol is related to presence of $-OC_2H_5$ groups, and is explained in the previous section.

The high roughness in the GO structure is assumed to be related to the large, bulky particles formed in the coating synthesis. The high roughness contributes to a large surface area. If this affects bacteria growth, is not determined. The large surface area does increase the amount of oxide groups from GO on the surface. Assuming production of ROS is the antibacterial mechanism, a longer durability of anti-fouling effects will be provided.

In the surface profile plots in Figure 4.6, there are observed small peaks pointing out of the curve for C-100. Similar peaks are also observed for C-125 and C-150, but are not as easily detected due to noise. The peaks are presumably folds in the GO sheets, and are observed in the AFM color maps. GO can be assumed to be present in the top layer of the coating surface. EDS analysis show that silicon and oxygen are the abundant species at the coating surface, but there is a high uncertainty in detection of light elements, like carbon, in EDS analysis. In the AFM 3D image (Figure 4.5) C-ref provides random circular patterns on the surface. Why they occur might be related to deposition technique and heat treatment. They are not believed to affect the results.

## 5.5 General Evaluation of Results

From the material characterization, C-125 exhibit the best compromise regarding material utilization and desired surface properties. It provides a stable slurry, uniform surface and excellent mechanical properties.

Looking at the growth inhibiting properties, C-150 is found to be the most promising, with approximately 83% reduction in bacteria growth. C-125 and C-150 exhibit structural similarities, but for C-125, the growth of bacteria is reduced with approximately 50% for the same period of time. The reason for this is assumed to be explained by the probability of finding deviations in the coating structure, is lower for C-150 compared to C-125. C-150 show the lowest deviations in contact angles, provides less defects in the carbon structure and may therefore exhibit better anti-fouling properties.

# 6 Further Work

Interesting and promising results on the growth inhibiting properties of GO in anti-fouling coating applications were achieved in this work. However, the results are based on one successful experiment and the trends need further investigation to be confirmed. It is essential to coat the surface with a covering layer of GO for the best results, and it would be interesting to look at the possibilities to reduce material consumption. For better utilization, controlled incorporation of graphene oxide to the sol, and to investigate how the nanosheets are structured in the coating, is necessary.

The quantification method of produced biofilm is of high uncertainty in the conducted work, since it is based on a personal evaluation to find a representative surface area for bacteria growth. It would be interesting to do a fluorescence microscopy of the biofilm to determine the abundance of algal growth. Another possibility is to scratch off the surface layer and analyze it for biological matter.

In the determination of growth inhibiting properties the initial seawater stock should have the same concentration and type of bacteria in every experiment, keeping the biotic parameter constant. After the anti-fouling characteristics are established, the experimental set-up requires better adaption toward a realistic environments. This includes wider temperature and current ranges. Increasing the light access is also relevant to look at in further work.

Well developed CuO coatings are on the market for anti-fouling use and it would be of great relevance and interest to compare the antibacterial properties in GO and such CuO coatings.

Regarding the toxic effects of graphene materials, and the limited research on the topic, the EC50 value is a method for determination of a substance toxicity in living organisms and would be of interest to include in further studies.

Several parameters in the experimental procedure can be studied and optimised for better results. The sol synthesis, deposition technique, coating thickness and heat treatment all effects the physical and chemical properties on the coating surface.

Further attention should be drawn into changing the coating system, as the silica coating

does not provide the mechanical properties or performance required for use in marine industries. A coating system that might be studied is $Al_2O_3$ with a GO-additive. Finally, further material choices should be justified by environmental effects and by focus on sustainability.

# 7 Conclusion

The experimental procedure in this work proved successful to prepare a GO coating suitable for determination of the anti-fouling properties in GO.

Synthesis of silica sol have been studied for an acidic catalyst. The hydrolysis step was the dominating step in the synthesis, providing long chained polymers and a final dense coating. For GO coatings, spray coating were found to work well as a coating deposition technique, and three layers provided a homogeneous surface structure avoiding crack formation. The coating synthesis route was not preferred for CuO coatings and the additive endured agglomeration. The conducted results on the two additives were not comparable.

From characterisation work of the GO coating slurries, GO show better stability in slurry when it was added in higher concentrations. This was assumed to be a result from both electrostatic repulsion and steric hindrance. There were found a linear trend between GO concentration and amount of defects in carbon structure, based on Raman spectra and peak intensity ratio between D and G peaks in the xerogels. The defects are observed to decrease with increasing GO concentration.

Based on the micro scratch tests, it can be concluded that increasing GO concentration in coatings result in enhanced adhesion strength and an increased wear resistance. GO show good adhesion properties to both 316 SS and PE, the utilized substrate materials in this work.

The biofilm development was visibly reduced when GO was added to the coatings. This was observed in the long term experiment, comparing number of bacteria on samples between week one and two in the experiment. C-150 provided the best growth inhibiting properties, and reduced the number of bacteria with $\sim 83\%$. Finally, it can be concluded that the GO additive show promising properties regarding antibacterial activity and utilization in anti-fouling coating application.

# Bibliography


[1] Nina Blöcher. *About biofouling*. Oct. 2019. URL: https://www.sintef.no/en/ocean/initiatives/biofouling/about-biofouling/.

[2] *Notvasksystemer*. Dec. 2019. URL: https://www.akvagroup.com/merdbasert-oppdrett/notvasksystemer.

[3] *Membrane biofouling*. Nov. 2019. URL: http://www.global-membrane.com/biofouling/%20membrane-biofouling/..

[4] *Understanding marine biofouling: How anti-fouling systems prevent growth*. Jan. 2020. URL: https://safety4sea.com/cm-understanding-marine-biofouling-how-anti-fouling-systems-prevent-growth/.

[5] Sunde, L.,M., Olafsen, K., Nordtug. *Tiltak for å begrense kobberbruk i havbruk - optimalisere metoder for å impregnere not Sluttrapport*. 2008.

[6] Srinivasan, M., Swain, G. "Managing the Use of Copper-Based Antifouling Paints". In: *Environmental Management* 39.3 (2007), pp. 423–41.

[7] Jastrzebska, A. M., Kurtycz, P., Olszyna, A. R. "Recent advances in graphene family materials toxicity investigations." In: *Journal of Nanoparticle Research* 14.12 (2012), p. 1320.

[8] Liu, S., Zeng, T. H., Hofmann, M., Burcombe, E., Wei, J., Jiang, R., Kong, J., & Chen, Y. "Antibacterial activity of graphite, graphite oxide, graphene oxide, and reduced graphene oxide: membrane and oxidative stress." In: *ACS nano* 5.9 (2011), pp. 6971–6980.

[9] Park, S., Mohanty, N., Suk, J. W., Nagaraja, A., An, J., Piner, R. D., Cai, W., Dreyer, D. R. and Berry, V., & Ruoff, R. S. "Biocompatible, robust free-standing paper composed of a tween/graphene composite." In: *Advanced Materials* 22.15 (2010), pp. 1736–1740.

[10] Sandbakk, S. *Coatings for Anti-Fouling Application: Addition of Graphene Oxide to a Hydrophilic Silica Coating*. 2019.

[11] Dürr, S., Thomason, J.,C. *Biofouling*. Blackwell Publishing Ltd, 2010.

[12] Zobell, C.E. "The effect of solid surfaces upon bacterial activity". In: *Journal of Bacteriology* 46 (1943), pp. 39–56.

[13] Lewandowski, Z. *Structure and function of biofilms. In: Biofilms: Recent Advances in their Study and Control (ed. L.V. Evans)*. Amsterdam: Harwood Academic Publishers, 2000.

[14] Jenkins, S., R., Martins, G., M. *Succession on Hard Substrata, chapter 4. In: Biofilms (ed. S. Dürr)*. Blackwell Publishing Ltd, 2010.

[15] Wahl,M. *Living attached: aufwuchs, fouling, epibiosis. In: Fouling Organisms of the Indian Ocean: Biology and Control Technology (eds R. Nagabhushanam & M. Thompson)*. New Delhi: Oxford & IBH Publishing, 1997.

[16] Railkin, A.I. *Marine Biofouling: Colonization Processes and Defenses.* CRC Press, Boca Raton., 2004.

[17] Cooksey, K.E. & Wigglesworth-Cooksey, B. "Adhesion of bacteria and diatoms to surfaces in the sea: a review." In: *Aquatic Microbial Ecololgy* 9 (1995), pp. 87–96.

[18] Maki,J.S. *Biofouling in the marine environment. In: Encyclopedia of Environmental Micro biology (ed. G. Bitton)*. New York: John Wiley & Sons, 2002.

[19] Flemming, H.-C., Wingender, J., Griebe, T. & Mayer C. *Physico-chemical properties of biofilms. In: Biofilms: Recent Advances in their Study and Control (ed. L.V. Evans)*. Amsterdam: Harwood Academic Publishers, 2001.

[20] McEldowney, S. & Fletcher, M. "Effect of growth conditions and surface characteristics of aquatic bacteria on their attachment to solid surfaces." In: *Journal of Dental Microbiology* 132 (1986), pp. 513–523.

[21] K. Schacht, U. Slotta, M. Suhre. "Prevention of Biofilm Formation with Vegan Silk Polypeptides". In: *sofw Journal* 143 (2017).

[22] Costeron, J.W., Lewandowski, Z., Caldwell, D.E., Korber, D.R. & Lappin-Scott, H.M. "Microbial biofilms". In: *Annual Review Microbiology* 49 (1995), pp. 711–745.

[23] Cao, R.S. & Alaerts, G.J. "Influence of reactor type and shear stress on aerobic biofilm morphology, population and kinetics." In: *Water Research* 29 (1995), pp. 107–118.

[24] Acuña, N., Ortega-Morales, B.O. & Valadez-González, A. "Biofilm Colonization Dynamics and Its Influence on the Corrosion Resistance of Austenitic UNS S31603 Stainless Steel Exposed to Gulf of Mexico Seawater". In: *Mar Biotechnol* 8 (2006), pp. 62–70.

[25] Ferrari, A. C., Bonaccorso, F., Fal'Ko, V., Novoselov, K. S., Roche, S., Bøggild, P., Borini, S. and Koppens, F. H., Palermo, V., Pugno, N. "Science and technology roadmap for graphene, related two-dimensional crystals, and hybrid systems". In: *Nanoscale* 7.11 (2015), pp. 4598–4810.

[26] Huang, H., De Silva, K., Kumara, G.R.A. et al. "Structural Evolution of Hydrothermally Derived Reduced Graphene Oxide". In: *Scientific Reports* 8.6849 (2018).

[27] Young, R. J., Kinloch, I. A., Gong, L., & Novoselov, K. S. "The mechanics of graphene nanocomposites: a review." In: *Composites Science and Technology,* 74.12 (2012), pp. 1459–1476.

[28] Vadukumpully, S., Paul, J., Mahanta, N., & Valiyaveettil, S. "Flexible conductive graphene/poly (vinyl chloride) composite thin films with high mechanical strength and thermal stability." In: *Carbon* 49.1 (2011), pp. 198–205.

[29] Walker, L. S., Marotto, V. R., Rafiee, M. A., Koratkar, N., & Corral, E. L. "Toughening in graphene ceramic composites." In: *ACS Nano* 5.4 (2011), pp. 3182–3190.

[30] Neklyudov, V. V., Khafizov, N. R., Sedov, I. A., & Dimiev, A. M. "New insights into the solubility of graphene oxide in water and alcohols." In: *Physical Chemistry Chemical Physics* 19.26 (2017), pp. 17000–17008.

[31] Cao, N., Zhang, Y. "Study of Reduced Graphene Oxide Preparation by Hummers' Method and Related Characterization". In: *Journal of Nanomaterials* (2015).

[32] Preben C. Mørk. *Overflate og Kolloidkjemi*. 8th ed. Institutt for kjemisk prosessteknologi, 2004.

[33] Islam, M.S., Anindya, K.N., Bhuiyan, A.G. et al. "Deconvolution of Raman spectra of disordered monolayer graphene: an approach to probe the phonon modes." In: *Bull Mater Sci* 42.147 (2019).

[34] Wu, J-B., L.,M-L., Cong, X., Liu, H-N,Tan, P-H. "Raman spectroscopy of graphene-based materials and its applications in related devices". In: *Chem. Soc. Rev.* 47 (2018), pp. 1822–1873.

[35] Jansson, P. A. *Deconvolution. With applications in spectroscopy*. Orlando: Academic Press.

[36] C. Jeffery Brinker and Scherer, George W. *Sol-Gel science: the physics and chemistry of sol-gel processing*. Boston: Academic Press, 1990. ISBN: 0-12-134970.

[37] C. J. Brinker. "Hydrolysis and condensation of silicates: effects on structure." In: 100.1-3 (1988), pp. 31–50.

[38] A. Feinle, M. S. Elsaesser, and N. Hüsing. "Sol–gel synthesis of monolithic materials with hierarchical porosity". In: *Chem. Soc. Rev.* 45.12 (2016). Publisher: The Royal Society of Chemistry, pp. 3377–3399. DOI: 10.1039/C5CS00710K. URL: http://dx.doi.org/10.1039/C5CS00710K.

[39] Vossen, J. L., Kern, W., Kern, W. *Thin film processes II*. Vol. 2. Gulf Proffesional Publishing, 1991.

[40] Jenkner, P. Monkiewicz, J. Beari, F. Siesler, H. W. Metternich, H. J. Brand, M. Lehnert, R. "Organofunctional alkoxysilanes in dilute aqueous solution: new accounts on the dynamic structural mutability." In: 625.2 (2001), pp. 208–216.

[41] European Union. "European Directive 98/8/EC of the European Parliament and of the Council of 16 February 1998 concerning the placing of biocidal products on the market". In: *Official Journal of the European Union* L123/1 (1998).

[42] Selim, M. S., Shenashen, M. A., El-Safty, S. A., Higazy, S. A., Selim, M. M., Isago, H., & Elmarakbi and A. "Recent progress in marine foul-release polymeric nanocomposite coatings." In: *Progress in Materials Science* 87 (), pp. 1–32.

[43] R.MorentN.De Geyter. “Functional Textiles for Improved Performance, Protection and Health”. In: (2011), pp. 3–26.

[44] Ye, L., Zhang, Y., Song, C., Li, Y., Jiang, B. “A simple sol-gel method to prepare superhydrophilic silica coatings.” In: *Materials Letters* 188 (2017), pp. 316–318.

[45] Isabel Jiménez-Pardo et al. “Hydrophilic Self-Replenishing Coatings with Long-Term Water Stability for Anti-Fouling Applications”. In: *Coatings* 8.5 (2018). ISSN: 2079-6412. DOI: 10.3390/coatings8050184.

[46] R.N. Wenzel. “Resistance of solid surfaces to wetting by water”. In: *Ind. Eng. Chem* 28 (1936).

[47] Biolin Scientific. *Prescision tensiometers*. Aug. 2020. URL: https://www.biolinscientific.com/attension.

[48] *The Measurement of Surface Finish*. Aug. 2020. URL: http://www.tarkkuustuonti.fi/Kampanjat/Brochure_Metrology_Surface_Parameter.pdf.

[49] Nanosurf AG. *Operating Instructions easyScan 2 AFM Version 1.6*. Aug. 2020. URL: https://www.usna.edu/Users/physics/vanhoy/_files/SP425/LabDocs/STM/Installation%20CD/Manuals/easyScan%202%20AFM%20Operating%20Instructions.pdf.

[50] United States. Army Materiel Command. *Maintainability Guide for Design*. 1972.

[51] Anton Paar. *Scratch resistance of coatings*. Apr. 2020. URL: https://wiki.anton-paar.com/en/scratch-resistance-of-coatings/.

[52] Perednis, D. Gauckler, L. J. “Thin film deposition using spray pyrolysis”. In: *Journal of electroceramics* 14.2 (2005), pp. 103–111.

[53] Liu, Y., Wen, J., Gao,Y. et al. “Antibacterial graphene oxide coatings on polymer substrate”. In: *Applied Surface Science* 436 (2017), pp. 624–630.

[54] Zhang, W., Wang, C., Li, Z. “Unraveling Stress-Induced Toxicity Properties of Graphene Oxide and the Underlying Mechanism”. In: *Advanced Materials* 9 (2012), pp. 5391–5397.

[55] Nguyen, H. N., Rodrigues, D. F. “Chronic toxicity of graphene and graphene oxide in sequencing batch bioreactors: A comparative investigation”. In: *Journal of Hazardous Materials* 343 (2018).

[56] O. Akhavan, E. Ghaderi. “Toxicity of graphene and graphene oxide nanowalls against bacteria”. In: *ACS Nano* 4 (2010), pp. 6971–6980.

[57] X. Zou, L. Zhang, Z. Wang, Y. Luo. “Mechanisms of the antimicrobial activities of graphene materials”. In: *J. Am. Chem. Soc.* 138 (2016), pp. 2064–2077.

[58] W. Hu, C. Peng, W. Luo, M. Lv, X. Li, D. Li, Q. Huang, C. Fan. “Graphene-based antibacterial paper”. In: *ACS nano* 4 (2010), pp. 4317–4323.

[59] S. Liu, T.H. Zeng, M. Hofmann, E. Burcombe, J. Wei, R. Jiang, J. Kong, Y. Chen. “Antibacterial activity of graphite, graphite oxide, graphene oxide, and reduced graphene oxide: membrane and oxidative stress”. In: *ACS Nano* 5 (2011), pp. 4317–4323.

[60] William Rise. *Coatings with Antifouling Properties due to Graphene Oxide Addition*. Tech. rep. June 2019.

[61] Huang, H., De Silva, K., Kumara, G.R.A. et al. "Structural Evolution of Hydrothermally Derived Reduced Graphene Oxide". In: *Sci Rep* 8 (2018).

[62] Soomro, S. A., Gul, I. H., Naseer, H., Marwat, S., Mujahid., M. "Improved performance of CuFe2O4/rGO nanohybrid as an anode material for lithium-ion batteries prepared via facile one step method". In: *Current Nanoscience* 15 (2019), pp. 420–429.

[63] Krishnamoorthy, K., Veerapandian, M., Yun, K. & Kim, S. J. "The chemical and structural analysis of graphene oxide with different degrees of oxidation". In: *Carbon* 53 (2013), pp. 38–49.

[64] Chua, C. K. & Pumera, M. "Chemical reduction of graphene oxide: a synthetic chemistry viewpoint". In: *Chem. Soc. Rev.* 43 (2014), pp. 291–312.

[65] Niggli, P. "Die Kristallstruktur einiger Oxyde I." In: 57 (1922), pp. 253–299.

[66] MubarakAli, D., Jagadheesan, A., Pratheesh, P., et al. "Synthesis and characterization of biocompatible tenorite nanoparticles and potential property against biofilm formation". In: *Saudi Pharmaceutical Journal* 23.4 (2014).

[67] Jaworski, S., Wierzbicki, M., Saworz, E., Chwalibog, A., et al. "Graphene Oxide-Based Nanocomposites Decorated with Silver Nanoparticles as an Antibacterial Agent". In: *Nanoscale Research Letters* 13.1 (2018).

[68] Pieper, H., Chercheja, S., Eigler, S. et al. "Endoperoxides Reveald as Origin of the Toxicity of Graphene Oxide". In: *Angewandte Chemie Int. Ed.* 55 (2016), pp. 405–407.

[69] Ye, S., Feng, J. "The effect of sonication treatment of graphene oxide on the mechanical properties of the assembled films". In: *RSC Advances* 6.46 (2016), pp. 39681–39687.

[70] Marsh, H., Rodríguez-Reinoso, F. *Activated Carbon*. Elsevier Science, 2006. ISBN: 978-0-08-044463-5.

# Appendices

# A Calculations

## A.1 Chemical composition in silica sol

Table A.1 shows the material properties of the chemicals used in the sol synthesis. The volume of each chemical component was found by Equation (A.1).

**Table A.1:** Chemical properties

| Chemical | wt% | Molar ratio | Molar mass [g/mol] | Density [g/mL] |
|---|---|---|---|---|
| TEOS | 98 | 1 | 208.33 | 0.933 |
| EtOH | 99,97 | 36.8 | 46.07 | 0.790 |
| DIW | 1 | 4 | 18.02 | 0.998 |
| HCl | 32 | 0.01 | 36.46 | 1.18 |

$$V_{component}[mL] = \frac{Mm \cdot n}{\delta \cdot wt\%} \tag{A.1}$$

Where $Mm$ is molar mass, $n$ is number of moles and $\delta$ is the density. The number of moles TEOS was set before calculations (dependent of wanted volume of the finished sol), and the other moles were calculated from this by Equation (A.2), where $r$ is the molar ratio.

$$n_{component}[mol] = r \cdot n_{TEOS} \tag{A.2}$$

## A.2 Coating synthesis

To determine the volume of GO stock solution to be added to the sol, Equations (A.4)-(A.6) were used.

$$m_{tot,TEOS}[g] = wt\%_{TEOS} \cdot \delta_{TEOS} \cdot V_{TEOS} \tag{A.3}$$

Equation (A.3) calculates the mass of TEOS in the total volume of sol. For coating synthesis, 10 mL of sol was extracted from the total volume, for each coating made. An

homogeneous mix was assumed.

$$m_{TEOS}[g] = \frac{m_{tot,TEOS}}{V_{tot}} \cdot V_{TEOS} \tag{A.4}$$

The mass calculated in Equation (A.4) is the mass of TEOS in the 10 mL ($V_TEOS$) of extracted sol. The masses of GO to be added, were found by multiplying with the wanted TEOS/GO weight ratio ($wr$) found in Table 3.1.

$$m_{GO}[g] = m_{TEOS} \cdot wr \tag{A.5}$$

$$V_{GO}[mL] = \frac{m_{GO}}{c_{GO}} \tag{A.6}$$

The volume of GO stock solution added to the sol was calculated by Equation (A.6), where $c_{GO}$ is the concentration [g/mL] of GO in the stock solution.

# B GO Technical Data Sheet

Transmission Electron Microscopy (TEM) image, electron diffraction and chemical composition from EDS for 10wt% aqueous graphene oxide paste, was provided in a technical data sheet from supplier, CealTech AS. TEM image and electron diffraction are given in Figure B.1, and EDS results in Table B.1.

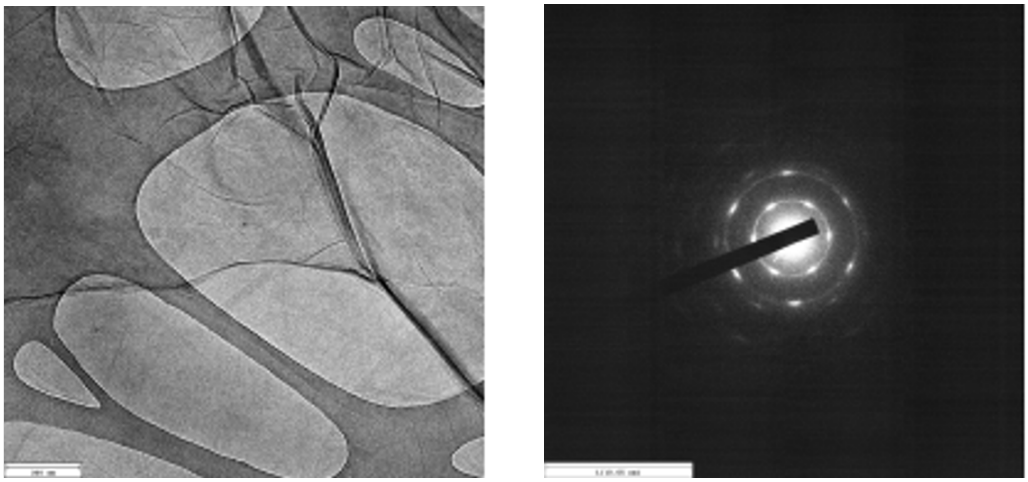

**(a)** TEM **(b)** Electron Diffraction

**Figure B.1:** a) TEM image and b) eletron diffaction image of 10wt% aqueous graphene oxide paste.

**Table B.1:** Chemical composition in 10wt% aqueous graphene oxide paste.

| Element | Weight % | Atomic% |
|---|---|---|
| Carbon | 55.41 | 62.38 |
| Oxygen | 44.43 | 37.55 |
| Sulfur | 0.1 | 0.004 |
| Chloride | 0.004 | 0.002 |
| Metal | Not Detected | |

# C Slurry Stability

From the specialization project, the slurry stability was identified by slurry appearance and by measuring zeta potential. At the stage where graphene oxide was added to sol in different concentrations, it was observed that slurry stability was more durable for higher concentrations of GO, as illustrated in Figure C.1. This observation required further investigation of the electrostatic properties of the suspensions. The zeta potential was measured, and the results in Table C.1 show that the stability increases by increasing GO/TEOS weight ratio. Coating IDs and associated GO/TEOS ratio for each slurry are explained in the table. The definition of a stable dispersion is below -30 mV (or above 30 mV) and C-001 (represent C-100 in present thesis) is found to be close to the stable range [32].

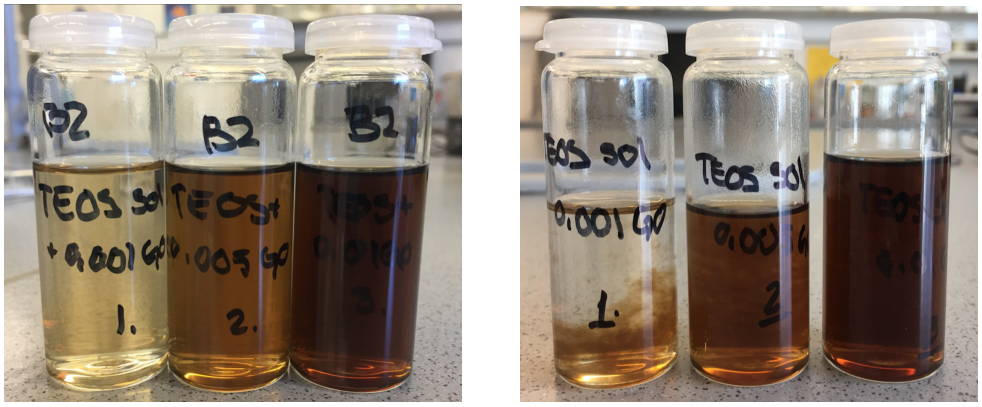

**Figure C.1:** The difference in suspension stability in C-0001, C-0005 and C-001 (left to right). The left image show the dispersion after being shaken and the right image is 24 h later.

**Table C.1:** The measured zeta potential for the slurries. The pH in the dispersions is 6.

| Coating ID | GO/TEOS weight ratio | Zeta potential [mV] |
|---|---|---|
| C-0001 | 0.001 | -20.81 |
| C-005 | 0.005 | -27.75 |
| C-001 | 0.01 | -28.08 |

# D Coating Surface Structure

Figure D.1 provide SEM images of six layers coated samples. The images are adapted from the specialization project and prove that high coating thickness provoke crack formation. The GO/TEOS weight ratio for associated Coating ID is included in Table C.1.

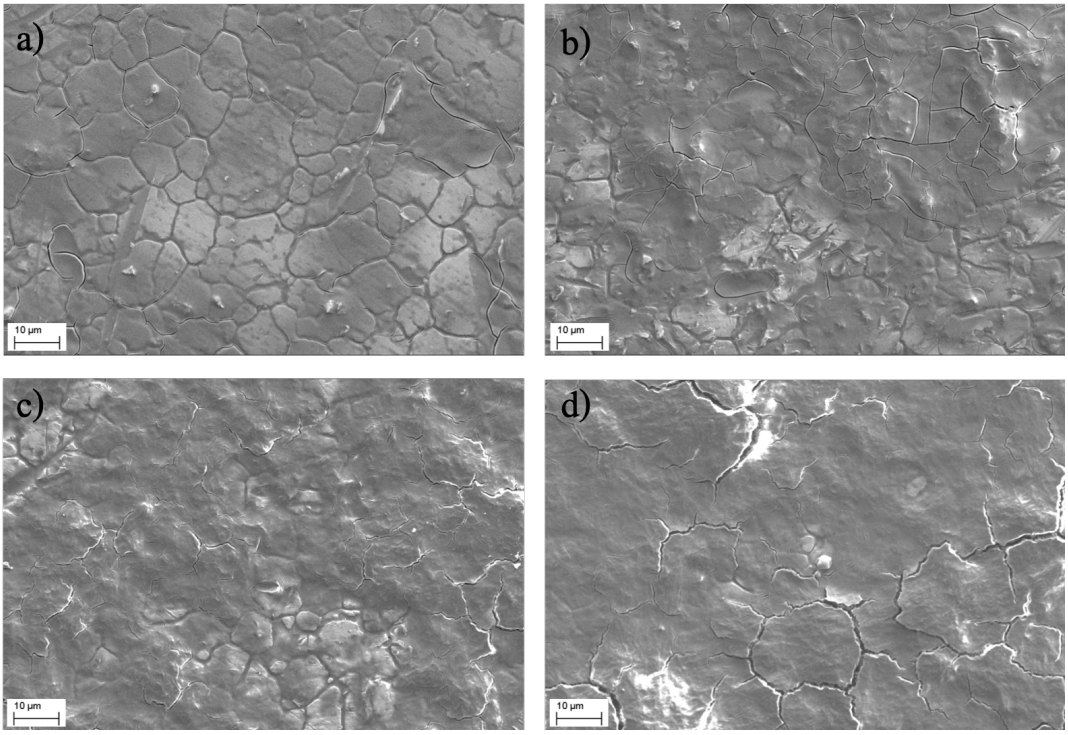


**Figure D.1:** Images six layers coated surfaces. a) C-Ref, b) C-0001, c) C-0005 and d) C-001.

# E Contact Angle Measurements

Wetting properties were determined for all GO and reference coatings, on steel substrates coated in 1-5 layers and are given in Figure E.1 The bar chart include error bars, and show the lowest deviation of contact angles for C-150. C-125 and C-150 exhibit similar wetting properties for all layers.

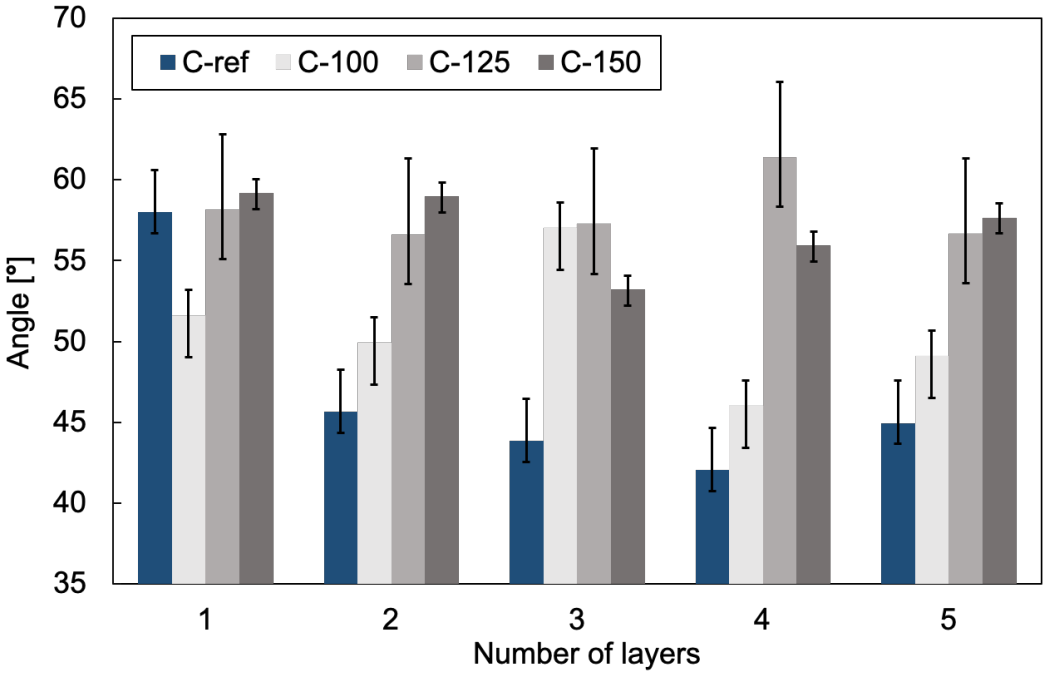


**Figure E.1:** Contact angles for reference and GO coated surfaces. The plot show wetting properties for coatings applied in 1-5 layers.

# F Micro Scratch Tests

Micro scratch tests were run on all steel samples coated with three layers of GO and reference coatings. The plotted scratch profiles are given in Figure F.1. C-125 are found to exhibit the highest adhesion strength. Generally, the wear resistance is highly improved by additions of GO in coating. The recovery for each coating is provided in Figure F.2

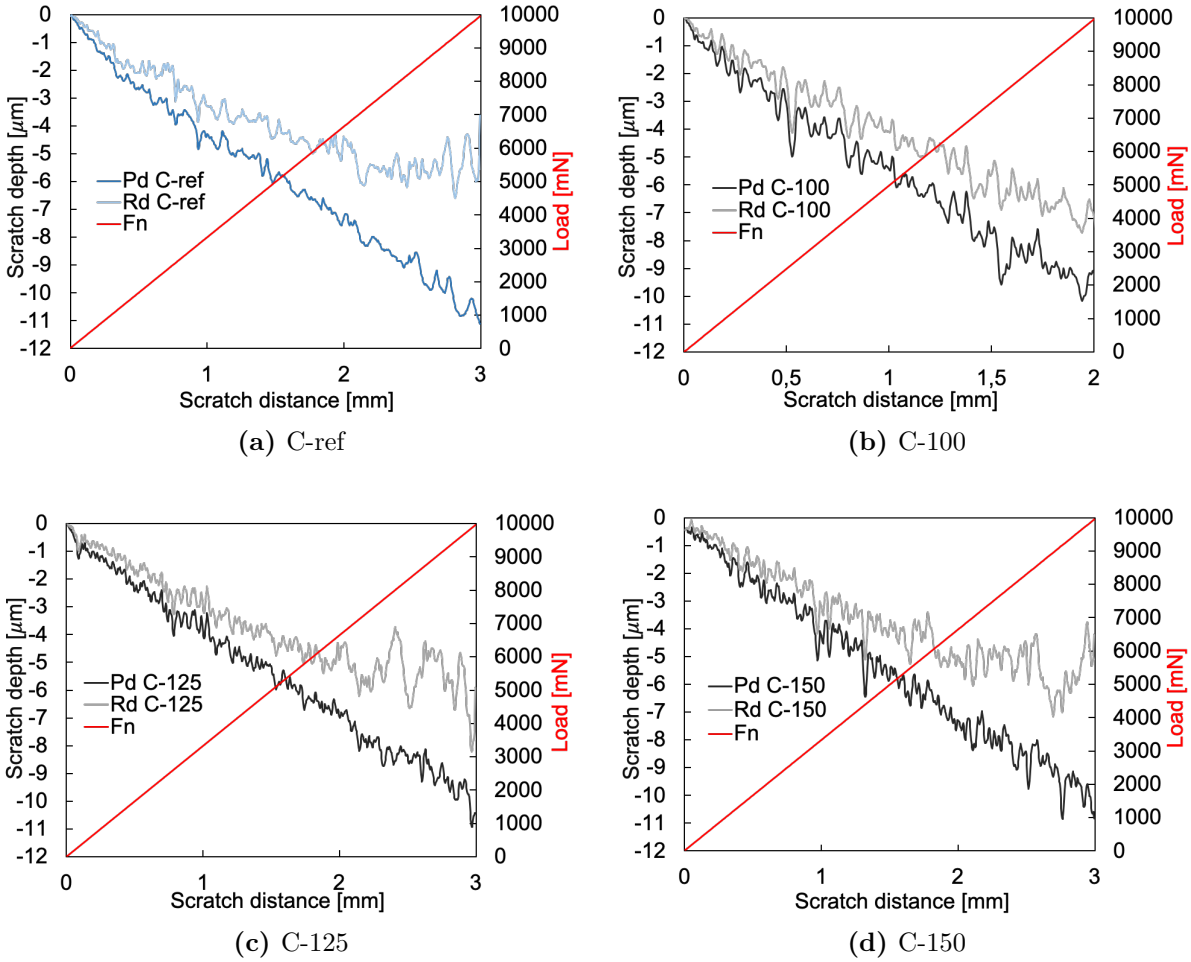


**(a)** C-ref **(b)** C-100

**(c)** C-125 **(d)** C-150

**Figure F.1:** Scratch penetration depth ($P_d$) at progressive load (30-10,000 mN) and residual depth ($R_d$) at constant load (30 mN) for a) C-ref and b) C-100, c) C-125 and d) C-150 over a distance of 3 mm.

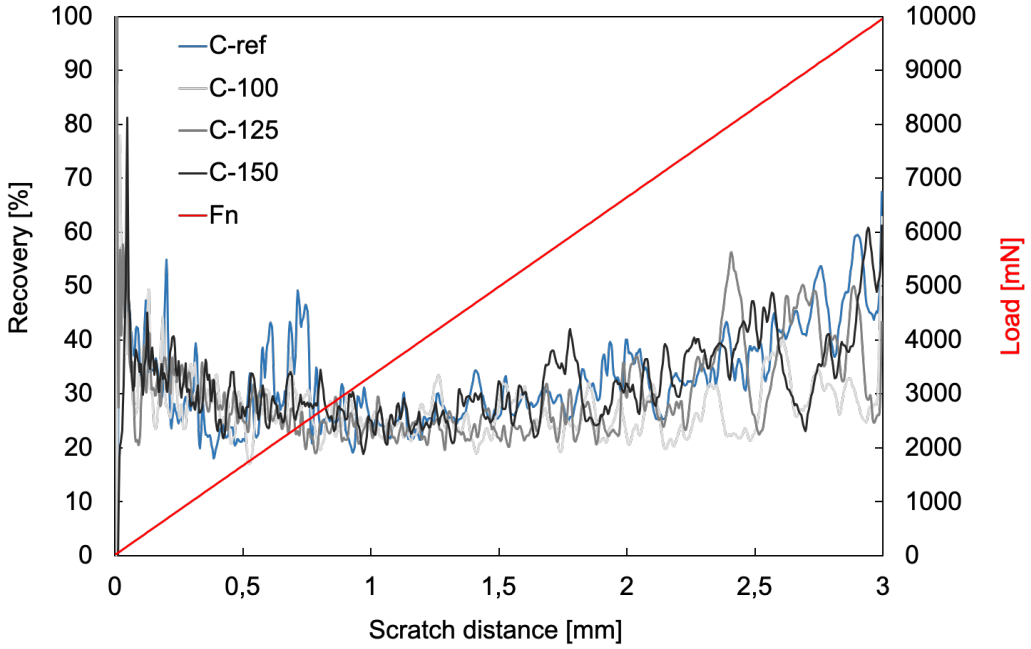


**Figure F.2:** % recovery for the corresponding coating samples in Figure F.1.